A Silicon-Pixel Paradigm for PET

Aleix Boquet-Pujadas, *Member, IEEE*, Jihad Saidi, Mateus Vicente, Lorenzo Paolozzi, Jonathan Dong, Pol del Aguila Pla, Giuseppe Iacobucci, and Michael Unser, *Life Fellow, IEEE*

***Abstract*—Positron emission tomography (PET) scanners use scintillation crystals to stop high-energy photons. The ensuing lower-energy photons are then detected via photomultipliers. We study the performance of a stack of monolithic silicon-pixel detectors as an alternative to the combination of crystals and photomultipliers. The resulting design allows for pitches as small as 100 μm and greatly mitigates depth-of-interaction problems. We develop a theory to optimize the sensitivity of these and other scanners under design constraints. The insight is complemented by Monte Carlo simulations and reconstructions thereof. Experiments and theory alike suggest that our approach has the potential to move PET closer to the microscopic scale. The volumetric resolution is an order of magnitude better than that of the state of the art and the parallax error is very small. A small-animal scanner is now under construction.**

***Index Terms*—Depth of interaction (DOI), monolithic active-pixel sensors (MAPS), optimization, positron emission tomography (PET), sensitivity, small-animal.**

I. Introduction

THE RESOLUTION of positron emission tomography (PET) has evolved hand in hand with scintillator technology since the 1950s [1]. Advances in manufacturing techniques have allowed for scintillation crystals with a better balance between (photon) stopping power, signal output, and decay time. They have also enabled the miniaturization of crystals into arrays of increasingly smaller pitch [2]. Photon detectors—and the electronics therein—are another key component of PET scanners because they measure the scintillation of the crystals. Accordingly, breakthroughs in detector technology have translated into scanner improvements too [1]. For example, photo-multiplier tubes are being replaced by faster and smaller solid-state photodetectors, while the addition of dual-side-readout electronics is improving depth-of-interaction (DOI) accuracy [3], [4].

The particle-physics community has developed silicon-pixel detectors [5], [6], [7]. They are used in many experiments, such as in those performed at CERN's Large-Hadron Collider [8]. A promising generation of silicon detectors is based on monolithic active-pixel sensors (MAPS), wherein the sensor is embedded directly onto the same silicon substrate as the CMOS readout electronics [9], [10]. In contrast to hybrid detectors, the lack of the expensive die-to-die interconnection in MAPS simplifies the assembly process, reducing production costs while allowing for great miniaturization.

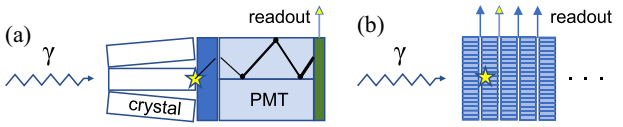

Fig. 1. Comparison between paradigms. (a) In current technologies, a crystal stops the high-energy photon. The resulting lower-energy photons are then detected via a photomultiplier tube. (b) Silicon pixels with individual readouts stacked in layers (five layers are shown). Compton and photoelectric interactions with the Si generate a photoelectron that is detected by pixel diodes. The photon is not necessarily stopped. The separation between pixels is marked by horizontal lines. Relative sizes between the crystals in (a) and the detectors in (b) are scaled according to the smallest in the state of the art.

In this article, we argue that the MAPS technology is now mature enough to be applied to PET and to expand its current boundaries toward ultrahigh-resolution molecular imaging. We study a scanner configuration wherein MAPS are stacked in layers to accumulate sufficient "stopping" power. This is in replacement of both the scintillation crystals and the detectors deployed in conventional PET scanners [Fig. 1(a)]. The resulting paradigm has a detector pitch of 0.1 mm with a layer thickness of only 0.32 mm and a timing accuracy of 0.2 ns [Fig. 1(b)], all at a reasonable power consumption [11], [12]. MAPS also offer the possibility to trade pitch for timing.

We present a theoretical framework to optimize the sensitivity and the resolution of our scanner. In particular, we propose an expression for the sensitivity in terms of the X-ray transform, which we then maximize under the design constraints of the scanner. We also assess the effects of an heterogeneous sensitivity by deriving a Cramér–Rao bound, and propose a model for the parallax error. Our theoretical approach can be applied to other scanners, too. We validate our predictions with Geant4-Allpix^2 Monte Carlo simulations that span from positron emission to pixel readout [13], [14].

Our results confirm the potential of MAPS in small-animal PET scanners. For a scanner with a transaxial field of view (FOV) of 34 mm, a small diameter of 40 mm, and an axial coverage of 44 mm, we find an expected resolution of 0.22 mm at the center of the FOV, and of 0.24 mm close to the edges (15 mm off-axis). This is for Fluorine-18-labeled radiotracers and a filtered-back-projection reconstruction. The volumetric resolution is of 0.01 mm^3 at the center and of 0.014 mm^3 at

Manuscript received 10 April 2024; revised 17 July 2024; accepted 27 August 2024. Date of publication 9 September 2024; date of current version 5 February 2025. This work was supported by the Swiss National Science Foundation under Sinergia Grant CRSII5_198569. *(Corresponding author: Aleix Boquet-Pujadas.)*

This work did not involve human subjects or animals in its research.

Aleix Boquet-Pujadas and Jonathan Dong are with the Biomedical Imaging Group, École polytechnique fédérale de Lausanne, 1015 Lausanne, Switzerland (e-mail: aleix.boquetipujadas@epfl.ch).

Jihad Saidi, Mateus Vicente, Lorenzo Paolozzi, and Giuseppe Iacobucci are with the Département de Physique Nucléaire et Corpusculaire, University of Geneva, 1211 Geneva, Switzerland.

Pol del Aguila Pla and Michael Unser are with the Biomedical Imaging Group, École polytechnique fédérale de Lausanne, 1015 Lausanne, Switzerland, and also with the CIBM Center for Biomedical Imaging, 1015 Lausanne, Switzerland.

Color versions of one or more figures in this article are available at https://doi.org/10.1109/TRPMS.2024.3456241.

Digital Object Identifier 10.1109/TRPMS.2024.3456241

2469-7311 © 2024 IEEE. Personal use is permitted, but republication/redistribution requires IEEE permission.
See https://www.ieee.org/publications/rights/index.html for more information.

Authorized licensed use limited to: EPFL LAUSANNE. Downloaded on February 10,2025 at 10:31:15 UTC from IEEE Xplore. Restrictions apply.

15 mm. The sensitivity of the whole scanner ranges between 3.3% and 5.0% depending on the introduction of accessory "stopping" layers.

These simulations suggest that our configuration of silicon pixels could improve the volumetric resolution by an order of magnitude in comparison to the small-animal scanner prototypes with the best resolution in the state of the art (0.13–0.22 mm^3) [15], [16], [17], [18]. The timing resolution could potentially improve by one order, too. Perhaps the most enticing feature, however, is the DOI resolution (0.32 mm of layer thickness), which greatly reduces parallax errors. This prompted us to design the scanner with a very small diameter to profit from the small pixel pitch by minimizing acolinearity errors. Due to the peculiarities of the detection process, we are still working on being able to identify which photons scatter inside the FOV. Therefore, a factor to consider regarding the sensitivity is that we do not use an energy window.

As a result of this promising analysis, we have undertaken the task to build a prototype of the scanner (Fig. 2).

In Section II, we give an overview of the state of the art in small-animal PET. We continue with a detailed description of the scanner in Section III. We then study the resolution theoretically (Section IV). We follow with a general theory for the estimation and optimization of the sensitivity of the scanner in Section V. Finally, we perform simulations for validation and provide further insight in Sections VI and VII.

II. State of the Art in Small-Animal PET

Small-animal PET scanners are tailored to mice and rats for the purpose of preclinical studies. To achieve the same relative resolution that is common in clinical human scanners (2.5 mm for a 125-mm brain), a target resolution of 0.2 mm was deemed necessary for mice (with a 10-mm brain) by [2]. This is in coincidence with the resolution needed to study atherosclerotic plaques in mouse models of cardiovascular disease [19], but it might be insufficient to study the equivalent of some of the more intricate cerebral structures that are resolvable with the latest human-brain scanners (1.3 mm of resolution at the time of writing [20]).

The ensuing race for ultraresolution has brought experimental scanners to the half-millimeter mark. At the forefront, there are a few scanners boasting a resolution of 0.5–0.6 mm at the center of their FOV, albeit this worsens toward the edges [15], [16], [17]. Pinholes [15] or crystal arrays with small pitches of around 0.5 mm are used to this achievement. This results in a volumetric resolution of approximately 0.13–0.22 mm^3 at the center. The DOI resolutions of these scanners range between 1.7 and 5 mm. More recently, a scanner with an axial coverage that is long enough to image the entirety of the mouse brain reached 0.55 mm of resolution. It used crystal arrays in a DOI configuration with three layers [18]. There is also a proposition for a scanner that was projected to have a resolution better than 0.5 mm at a big diameter using Monte Carlo simulations [21]. A chart of several scanners can be found in [21]; we have also compiled some values in Table A1. For reference, current commercial scanners for mice range between 1 and 2 mm in resolution [2], or ~ 3 mm^3.

Even with the introduction of the NEMA standard, a fair comparison of scanners is not straightforward because the resolution depends on many variables, such as pitch, diameter, and even reconstruction method (see Table A1). For example, a wider diameter increases the acolinearity error, but it can decrease the parallax error if the FOV remains (intentionally) unchanged. This tradeoff of a wider diameter is more beneficial for bigger detectors. Note that our choice of tradeoff is in favor of a small diameter.

The sensitivities of PET scanners are difficult to compare, too, because of differences in energy windows and (axial and transaxial) coverage. The resolution of pinhole-based systems often comes at the price of reduced sensitivity [15]. Scanners based on small crystal pitches can also suffer in sensitivity due to small depths and low packing fractions [16], albeit some technologies do overcome these challenges [17], [18], [21].

III. Description of the Scanner

We now describe the scanner design investigated in this article. We note that some design parameters are only justified later (Sections IV and V) according to the optimization of resolution and sensitivity.

A. Characteristics of the Silicon Sensors

SiGe BiCMOS technology can produce MAPS with a pixel pitch of 0.1 mm, and with 0.02 ns of timing resolution [11]. We propose to arrange multiple 0.1-mm pitch pixel matrices into layers of length 60 mm and (axial) width 44 mm [Fig. 2(a) and (b)]. This amounts to $\sim 2.5 \cdot 10^5$ detection pixels per layer. Based on [11] and [12], we intentionally adopt a MAPS configuration with a worse [11] timing resolution of 0.2 ns in order to reduce power consumption to a level that scales to a whole scanner (see Appendix A). This corresponds to 4 μW per channel. A more conservative estimate for the final timing resolution upon construction is of 0.3 ns on account of the front-end electronics and system-level effects, such as calibration and layer synchronization. Each layer is made of 0.27 mm of Si on top of a flexible printed circuit (FPC), which can be manufactured to be anywhere between 0.05 and 0.2 mm. This translates into a potential thickness of only 0.32–0.47 mm per layer. An extra 0.05 mm of bismuth can be added on top of each layer to double the "stopping" power. For a single layer, the probability of detecting an orthogonal photon is 0.48%–0.73% (without, and with Bi). With stacks of 60 layers, we show later that the sensitivity of the whole scanner to a photon pair is roughly 3.3%–5.0% (without, and with Bi). The thin layering results in a very accurate DOI. The DOI is of special importance because it improves resolution in two ways: 1) by reducing parallax errors and 2) by allowing for the detectors of the scanner to be closer to the FOV, which in turn reduces acollinearity errors.

MAPS offer great scalability. Such technology allows for large areas of detectors to be manufactured commercially by very-large-scale integration processes. Therefore, silicon-pixel technology has now reached the right scale to make the scanner not only possible but also affordable.

B. Geometry of the Scanner

We designed the scanner rectangular to make it simple, scalable, and modular [22]. Other scanners with a "box" shape

Authorized licensed use limited to: EPFL LAUSANNE. Downloaded on February 10,2025 at 10:31:15 UTC from IEEE Xplore. Restrictions apply.

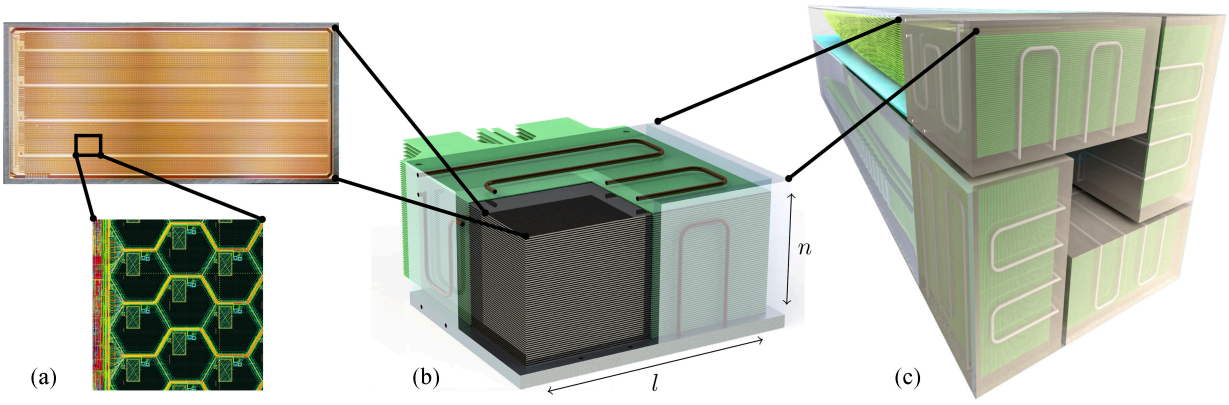

Fig. 2. Scanner. (a) Top: Microscopic image of an array of 0.1-mm pitch pixels manufactured for the scanner using SiGe BiCMOS. Bottom: Zoom-in of the electronic design showing seven (entire) pixels. (b) Block of 60 stacked layers (black) and their readout electronics (green). The pipes of the cooling system wind around the block. (c)) Scanner is made out of 4 blocks arranged around the FOV. Electrical connections (at the back) are also accounted for.

have been developed [23], [24], [25], [26]. We chose to make the sides overlap completely to improve the angular coverage. This design facilitates the integration of the cooling system and allows for a more uniform sampling of the FOV. The sensitivity maps resulting from the rectangular design are quite heterogeneous, but they can be compensated for in the reconstruction step. The excellent DOI makes this task easier.

The scanner consists of four rectangular detector blocks, each comprising $n = 60$ layers of length $l = 60$ mm [Fig. 2(b)]. The blocks are arranged with a rotational symmetry of 90° around the FOV [Fig. 2(c)], totaling $\sim 6 \cdot 10^7$ pixels. The radius of the transaxial FOV is $R_{\text{FOV}} = 17$ mm. A cooling system is wrapped around the detector blocks. In accordance with finite-element simulations, the cooling system is designed to dissipate the heat generated by the 240 W of power required to run the electronics in each block. Its casing is built in aluminum and is 3-mm thick [Fig. 2(c)]. This makes the scanner $2R = 40$ mm in diameter. While the cooling system introduces these small detector gaps of 6 mm between detector blocks, these gaps do not face the FOV and, therefore, do not result in significant sinogram gaps.

The 34 mm of transaxial FOV are meant to accommodate small mouse beds, which are often 30 mm in inner diameter [27], [Molecubes], [MR Solutions]. For example, they should fit mouse strains such as the common C57BL/6J; or the 129S1/SvJ and B6.129P2-*Apoe*^{tm1Unc}/J strains at standard dosing times of 8–12 weeks [28].

C. Detection Process and Energy Measurements

The detection process in our silicon-pixel scanner is not standard in PET. Instead, it is similar to that in a gas-ionization chamber. After an incident photon interacts in the scanner, the ensuing photoelectron loses its kinetic energy via ionization by generating electron–hole pairs in the crystal lattice of the silicon along its trajectory. These charges drift (and diffuse) toward the electrodes of the pixel, ultimately producing an electronic signal in the channel. The signal is proportional to the amount of charge which, in turn, is proportional to the energy deposited by the photon. It is possible that the random walk of the photoelectron crosses into contiguous pixels and ionizes them, too, albeit to a different degree. In such case, the location of the different pixels that are triggered can be combined by (possibly charge-weighted) averaging. This effect increases the apparent pitch size slightly (see Section VII-C), but the effect on the resolution is divided up into the three spatial dimensions.

The current in the pixel is measured by an analog-to-digital converter in time-over-threshold units, with a conservative resolution of 1 ns. This translates into a charge resolution of 200 electrons, or into an energy of $\sim$ 0.72 keV in silicon at 3.6 V per electron–hole pair. These energy measurements could be used to filter out noise (see Section VI-B), to assign cluster weights to the pixels, and to alleviate time-walk effects. However, we are still investigating how to distinguish events that scatter within the FOV, and how the front-end accuracy translates into the standard energy resolution quoted in PET. (Find the spectra in Appendix K.) For this article, we set a wide energy window of 10–850 keV that includes all interactions and we do not exploit the energy measurements any further.

Due to the energy regime and atomic number, most photons interact via Compton scattering in our scanner. The less energy they deposit, the less movement of the photoelectron across pixels, and the better the associated resolution (see Section VII-C). The very few photons that undergo photoelectric absorption instead deposit more energy. This worsens their corresponding spatial resolution because the resulting photoelectrons can move further across pixels. While we can resolve Compton interactions better, we include both kinds of interactions in our reconstructions. This is consistent with the wide energy window: our scanner does not aim at stopping photons, and Compton interactions can deposit small fractions of the energy of the photon.

In the vast majority of cases, the initial incident photon scatters once and then leaves our scanner without further interaction. Only a fraction of its energy is deposited and converted to signal. This is in contrast to standard PET scanners, which aim at stopping the incident photon entirely through the use of scintillators [2]. Even then, the scintillator-based scanners still suffer from intercrystal scattering, whereby different interactions caused by the same incident photon take place at different crystals and are difficult to disambiguate [29], [30], [31].

Authorized licensed use limited to: EPFL LAUSANNE. Downloaded on February 10,2025 at 10:31:15 UTC from IEEE Xplore. Restrictions apply.

Other semiconductors, such as CdTe or CdZnTe, have been used in PET scanners [32], [33]. In principle, their higher atomic number could provide more "stopping" power to our scanner, thereby increasing sensitivity. Notice that the photoelectron would lose energy faster, but there would be a higher proportion of photoelectric interactions. Unfortunately, there is no MAPS technology available for these materials. Hybrid approaches (such as bump-bonding a pixelated readout ASIC) result in worse DOIs at much higher prices and usually require bigger pitches.

The cost of building a prototype of our scanner is comparable to the price of commercial small-animal PET scanners (see Appendix B). The readout system is described in Appendix C.

IV. Theoretical Resolution

We now reconsider the limits of resolution of PET scanners [34], [35] in light of our proposal. This will explain many of our design choices and provide a quantitative comparison between silicon and scintillation-crystal technologies.

A. Limits of Resolution

We first review the limits imposed by physics.

1) Positron Range: Perhaps the most fundamental limit in PET is the mean free path (MFP) of positrons before they annihilate with an electron. This distance is a function of the initial kinetic energy of the positron and thus depends on the radiotracer. We chose the pixel pitch of the silicon detectors in accordance with the most common radiotracer, [^{18}F]fluorodeoxyglucose (FDG). At $r_{\mathrm{FWHM}} \approx 0.102$ mm of full width at half maximum (FWHM) [36], the MFP of FDG in water ranks among the smallest over many radiotracers. This value corresponds to the projection of the MFP onto the lines of response (LOR). In practice, the FWHM of the range of the positron is estimated by modeling the underlying distribution $r(x)$ as the sum of two exponentials for $x \geq 0$ [36], [37, eq. (16) and Table 1 (corrected units)]. Fitting this model to binned data is sensitive, which might explain the slight discrepancy of FWHMs across the literature [36], [38]. The positron limit may be (partially) overcome using deconvolution techniques [37]. Radiotracers with a bigger MFP will benefit less from the small pitch of our scanner.

2) Acollinearity: Photon pairs are not emitted in perfectly opposite directions upon annihilation. Instead, the angular momentum of electron and positron introduce an uncertainty with $\vartheta = 8$–10 mrad of FWHM [39] into the antiparallel assumption of $\pi\,rad$. This translates into a spatial error between LORs of $\sin(\vartheta/2)\,R \approx (\vartheta/2)R$, which corresponds to $a_{\mathrm{FWHM}} \approx 0.08$–$0.1$ mm for the first (and most-often hit) layer of our scanner. The distribution $a(x)$ of the acollinearity error is modeled as a Gaussian with standard deviation $a_{\mathrm{FWHM}}/\sqrt{8\ln 2}$.

The architecture of the scanner also affects the resolution.

3) Detector Pitch: The final resolution is tightly linked to the accuracy with which photons can be localized. This follows a triangular distribution $d(x) = d_{\mathrm{FWHM}} \max(0, 1 - |x/d_{\mathrm{FWHM}}|)$ with an FWHM of $p/2$, where p is the pitch of the pixels. The silicon-pixel design allows for detector pitches that compete with the FWHM of the physical limits. According to the combination of errors, (3), a sensible tradeoff is to set $p = 0.1$ to 0.2 mm (Fig. 3). Therefore, we chose 0.1 mm even though there exist smaller MAPS [40]. In comparison, the smallest pitches in crystal-based technology are 0.32, 0.43, and 0.5 mm in the most recent of experimental scanners [16], [17], [21].

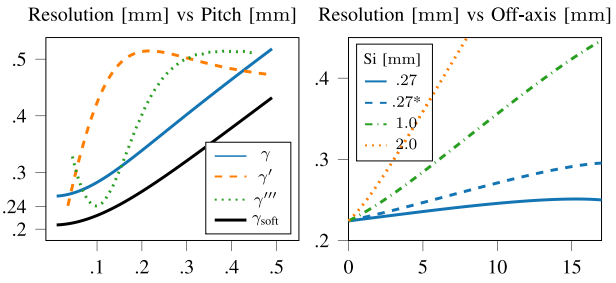

Fig. 3. Resolution optimization. Left: Resolution of the scanner according to (3) as a function of the pitch (smaller is better). The first and third derivatives (rescaled) portray the diminishing returns of making p smaller. All are in water [36], but γ_{soft} is in soft tissue [38]. Right: Theoretical resolution in (3) as a function of the sample distance ρ from the center in soft tissue. This is for a pitch of $p = 0.1$ mm and three different thicknesses of Si. They all have an added 0.05 mm of FPC (total thickness is h) except the one with the asterisk (0.2 mm).

4) Parallax Error: The miniaturization in width afforded by silicon also applies to depth. This results in a DOI between 0.32 and 0.47 mm. Silicon pixels with individual readouts can be made only 0.27-mm thick (or even less [40], [41]) and stacked in layers. An increase in the thickness of the FPC from 0.05 to 0.2 mm (Fig. 3) decreases the price of production with minor repercussions on off-axis resolution.

In contrast, crystal length is 5, 13, and 10–20 mm in the scanners [16], [17], [21]; albeit the latter two can measure the DOI of the photon with accuracies of only 1.7 and 1–2 mm by combining the crystal arrays with dual-ended readout DOI encoding modules.

DOI accuracy is important because it affects both radial and off-axis resolution. In conventional PET, photons are often assigned to the face of the crystal in which they are detected. However, when the sample is off-center, the angle of entry can be slanted enough for a photon to cross multiple crystals and be assigned to the wrong face. Another way to envision this radial elongation is to consider the apparent width of the detector. An approximation of the FWHM of this effect is $\alpha\rho/\sqrt{\rho^2 + R^2}$ in [35], where ρ is the sample offset and α is an experimental constant. We propose another approximation based on the observation that α should depend on the width p and h the thickness of the detector, as well as on ρ. By means of geometric arguments, this alternative perspective yields

$$d_{\mathrm{FWHM}} = \frac{h\rho}{2R} + \frac{p\sqrt{R^2 - \rho^2}}{2R}. \tag{1}$$

This includes the error $p/2$ of the detector pitch, which is recovered for $\rho = 0$. See Appendix D for more details. Note that $h/2$ could be approximated by the DOI resolution (FWHM) in other scanners, just as $p/2$ is the FWHM corresponding to half the apparent pitch.

With silicon pixels, the improvement in DOI accuracy effectively eliminates radial elongation (Fig. 3). As a consequence,

Authorized licensed use limited to: EPFL LAUSANNE. Downloaded on February 10,2025 at 10:31:15 UTC from IEEE Xplore. Restrictions apply.

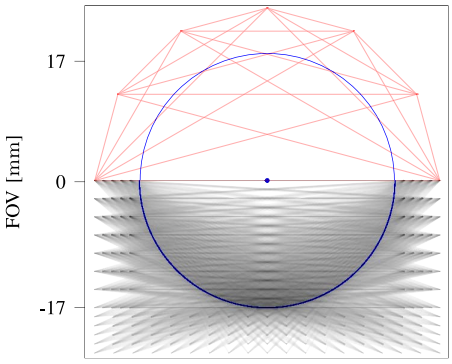

Fig. 4. Sampling uniformity. Sampling of the FOV (circle) by the LORs of a crystal-based scanner (positive FOV, top) and those of silicon pixels (negative FOV, top). The ratios between the DOI (and between) the pitch of the two scanners are accurate (to scale) and were taken from the "best" combination of features in the literature of crystal technology. Only the vertical sampling rate is well represented by the schematic because only half-scanners are shown for intelligibility. The circle-like geometry samples the center less than it does the edges, and the square-like geometry contains underlying uniform grids of parallel rays with specially high sensitivity. Both statements hold for the corresponding full scanners, albeit with less uniformity.

the resolution is practically uniform over the FOV, which means that the entire FOV is useful. In turn, this allows for more compact scanners with smaller acollinearity errors. In contrast, conventional PET scanners are made substantially larger than the FOV to mitigate further problems with the DOI [17], [21].

5) Nonuniform Sampling: The circular geometry of most PET scanners results in nonuniform sampling along the radial direction: less LORs per unit volume cross the center of the scanner than do the outside. Experimentally, this has been estimated to introduce a multiplicative factor of 1.25 to the FWHM [42]. Together with the DOI, the rectangular geometry of our proposed scanner greatly mitigates this effect (Fig. 4). In fact, a uniform grid is present within the sampling. The geometry, however, results in an unconventional sensitivity map in the sinogram domain (Section V).

6) Multiplexing: Some scanners multiplex several scintillation crystals onto the same photodetector. This is a consequence of the electronics becoming complex and costly. An experimental example of the resulting decoding effect came at the price of an FWHM of $p/3$ in [35]. Silicon pixels do not suffer from multiplexing because each detection pixel has its own readout-electronics channel.

Together, all uncertainties applicable to the silicon scanner combine into the distribution

$$\Gamma(x;\rho,p,R) \;= (r * a * d)(x) \tag{2}$$

with resolution

$$\gamma(\rho;p,R) \;= \mathrm{FWHM}\{\Gamma\}. \tag{3}$$

Expression (2) is based on the fact that the probability density function (pdf) of a sum of independent random variables is the convolution of their corresponding pdfs. See Appendix E for more details. While $(r * a)(x)$ admits an expression in terms of $\mathrm{erf}(x)$, further convolution with d does not seem to yield a closed-form expression.

Considering FDG, our small radius, the thin FPCs (where the parallax error is practically negligible), and a pitch between 0.1 and 0.15 mm (Fig. 3), we estimate that silicon-based scanners can operate with a best resolution of $\gamma \approx 0.28$–0.30 mm with the positron range in [36] for water, and of $\gamma \approx 0.22$–0.25 mm in soft tissue similarly to [38] (see Appendix H for a discussion about these two materials).

B. Noise and Uncertainty

We review four considerations that can affect the quality of reconstruction in terms of signal-to-noise ratio (SNR).

1) Time of Flight: At $\delta t \approx 0.2$–0.3 ns, the timing resolution of our silicon-based scanner remains too coarse for time-of-flight (TOF) methods. The diameter $2R_{\mathrm{FOV}} = 34$ mm of the FOV of the scanner is small relative to the potential localization distance $c\delta t/2 \approx 30$–45 mm. The improvement in SNR can be estimated to be $\mathrm{SNR}_{\mathrm{TOF}}/\mathrm{SNR}_{\neg\mathrm{TOF}} = \sqrt{4R_{\mathrm{FOV}}/c\delta t} \approx 1$ in the best-case scenario where R_{FOV} is also taken as the size of the measured specimen [43]. Note that the timing resolution of MAPS can be improved at the price of power consumption; this requires a calibration of the timing across pixels for maximal benefit.

2) Random Coincidences: With a timing resolution of 0.2–0.3 ns, random coincidences in silicon technology are much less prevalent than in crystal-based small-animal scanners. For example, the state-of-the-art conventional scanners in the previous comparisons manage timing resolutions of 4, 40, and 9.5 *ns* [16], [17], [18]. Since the number of coincidences scales in direct proportion to δt, random coincidences occur around one order of magnitude less frequently in our scanner. The result of fewer random coincidences is less noise, or a better SNR. This is especially interesting for higher radioactivity doses because the scattering fraction depends mostly on spatial distribution rather than on total activity.

3) Compton Scattering Inside of the FOV: As opposed to crystal technology, silicon pixels cannot yet tell apart photons that scatter within the FOV. However, the scattering fraction is low in small-animal scanners precisely because of their size. A naive calculation based on the mass attenuation coefficient of adipose tissue ($0.09\ \mathrm{cm}^{-1}$) at 511 keV yields $\exp(-0.09\ \mathrm{cm}^{-1} \cdot 1.7\ \mathrm{cm}) \approx 86\%$ of noninteracting photons.[1] In combination with the limited resolution of energy windows in crystals, this often makes scattering in small-animal scanners to be neglected or go unreported [46]. Typical scatter fractions are 8% and 17% for mice and rat phantoms, respectively [47].

4) Animal Movement: Experimental estimates of organ movement in mice are in line with our choice of pitch. For example, the movement of the abdominal and thoracic aortas amounts to 50 and 150 mm, respectively, between systole and diastole [48]. Whereas the radius of the renal one appears to stretch by 80 mm with a centroid motion of around 100 mm [49]. In comparison, atherosclerotic plaques—a potential target to study atherosclerosis with FDG—can

[1]Technically, all interactions are included therein, but it is still a very good approximation of Compton scattering because incoherent scattering dominates at this regime, cf. [44], [45, Table 4].

Authorized licensed use limited to: EPFL LAUSANNE. Downloaded on February 10,2025 at 10:31:15 UTC from IEEE Xplore. Restrictions apply.

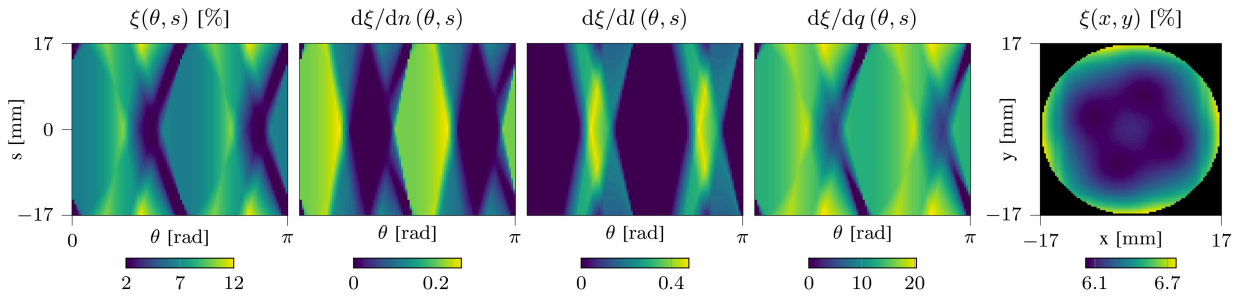

Fig. 5. Sensitivity and perturbations thereof (left to right): sensitivity in the sinogram domain (6); derivative of the sensitivity w.r.t. the number of layers (scaled to represent the change of adding 1 layer and amounting to an increase of 0.12% in average sensitivity); w.r.t. the length of the layers (adding 1 cm, 0.11%); w.r.t. λ (from $q = 0.0048$ to $2q$, 12.82% increase); and sensitivity on the FOV in the direct domain (8) with $\xi(x, y) = \bar{\xi}_{P_{x,y}}$. Colorbars are in %, θ is in *rad*, and x, y, and s are in mm.

reach more than 200 mm in thickness [19], [50]. Since most motion in sedated animals is periodic, they could be compensated during reconstruction. In fact, this is done for random movements in awake human patients [51]. Another perspective is gating. Gating can be implemented by detecting the motion from the acquisition itself (intrinsically) [52]. Or from complementary hardware (extrinsically), for example with electrocardiograms to compensate for the beating of the heart or with piezoelectric sensors [53], video cameras [54], [Sofie G8 PET/CT], or other devices to compensate for respiratory motion [55].

C. Transition to Human Scanners

The scanner radius necessary to fit a mouse, $R_{\text{FOV}} \approx 15$ mm [16], [17], [27], [28], and a human head, $R_{\text{FOV}} \approx 120$ mm, are close to one order of magnitude apart. This changes several of the design conclusions reached so far. With the acollinearity becoming the limiting factor at ~ 0.48 mm, a better tradeoff under power-consumption constraints is to increase the pitch size in exchange for better timing. Timings down to 20 ps have been achieved with silicon pixels in this way [11]. This could potentially be equivalent to 3 mm of in-LOR resolution and it could more than double the SNR. In lower-resolution systems, it would be enough to bypass tomographic reconstruction, as was done in [56] using collimation and Cherenkov radiation. At this radius, however, scattering would contribute a lot of noise to the measurements unless the photons are collimated. Future research will therefore focus on improving the detection of scattering to facilitate the scaling of our scanner to humans.

V. Theoretical Sensitivity

Since MAPS are new in PET, it is important to study how it affects the overall sensitivity. The rectangular geometry deserves attention too. To this end, we have derived an analytical expression for the probability of detection of any LOR within the FOV. There are two ingredients: 1) a model of the probability detection of photons and 2) the extension thereof to detector blocks using the X-ray transform. We use the expression for design optimization and for sinogram normalization.

A. Model of the Probability of Detection

Each silicon pixel has a measurable probability q of detecting an orthogonal hit by an annihilation photon. This probability is primarily a function of the attenuation caused by silicon, but it also depends on the thickness of the FPC and on the glue used to stack the layers. It can be measured experimentally or estimated through simulations. Our aim is to aggregate these effects into a single coefficient.

Each scanner block is organized in layers of pixels. The probability of detecting the orthogonal hit of a photon at layer m is therefore $(1-q)^{m-1}q$, and the cumulative probability is $\sum_{k=1}^{m}(1-q)^{k-1}q = (1-(1-q)^m)$. Consequently, $m \sim \text{Geo}(q)$. By taking the limit to infinitely thin layers, we extend the geometric distribution into a continuous exponential distribution $x \sim \text{Exp}(\lambda)$ in terms of the length x of the trajectory of the photon through the block. The equivalent rate λ is then the probability after a single layer of thickness h

$$\lambda = -\log(1-q)/h. \tag{4}$$

The corresponding cumulative distribution, $(1-e^{-\lambda x})$, recovers standard photon attenuation, but with an apparent coefficient. For our scanner, $q =$ 0.48%–0.73% (without, and with Bi). Depending on the FPC, this translates into a range of $\lambda =$ 1.4–$2.3{\cdot}10^{-2}\text{mm}^{-1}$ with Bi, and into $\lambda =$ 1.0–$1.8{\cdot}10^{-2}\text{mm}^{-1}$ without.

Adjusting the cumulative-probability formula to the detection of two photons, $(1-(1-q)^m)^2$, yields a naive upper bound of 6.3% for the sensitivity of the scanner with 60 layers and without Bi. In the next section, we will see that our (more accurate) modeling yields a lower estimate that is heterogeneous and in agreement with our subsequent simulations.

B. Sensitivity Map

We now extend the probability model to any LOR as parameterized by the sinogram variables (s, θ) of distance and angle. This entails two steps: 1) formulating the probability model for any line segment and 2) considering the detection of not only one, but two antiparallel photons.

We approach the probability model by using the X-ray transform $\mathcal{X}$. We consider a set of n_b detector blocks with domain $B_m \subset \mathbb{R}^d$ indexed by $m \in \mathbb{M} = \{0, \ldots, n_b - 1\}$, $d \in$

Authorized licensed use limited to: EPFL LAUSANNE. Downloaded on February 10,2025 at 10:31:15 UTC from IEEE Xplore. Restrictions apply.

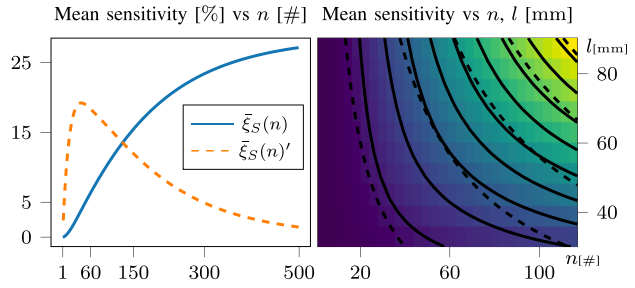

Fig. 6. Mean sensitivities. Left: Mean sensitivity (7) of the scanner as a function of the number of layers with fixed length. The derivative hints at the diminishing returns after 60 layers. Right: Depiction of the optimization problem (9). The underlying map displays the average sensitivity $\bar{\xi}_S$ w.r.t. the length and the number of layers (color map as in Fig. 5, but from 0% to 19.4%). Solid lines are isocontours of $\bar{\xi}_S$. Dashed lines are isocontours of $n \cdot l$, which acts as a constraint. As per the method of Lagrange multipliers, dashed lines are tangent to solid lines at optimal points.

$\{2, 3\}$. We model any heterogeneity of the material in the block with a weighting function $b_m(\mathbf{x}) : \mathbb{R}^d \to \mathbb{R}$ with $\text{supp} b_m \subset B_m$. We assume that the blocks are identical and arranged in $\varpi = 2\pi/n_b$ orientations around the FOV. This is formalized as $b_{m+1}(\mathbf{x}) = b_m(\mathbf{R}_\varpi \mathbf{x})$, where $\mathbf{R}_\varpi$ is the corresponding rotation matrix. The probability that the block B_m detects a photon along LOR (s, θ) is then

$$1 - \mathrm{e}^{-\lambda \mathcal{X}\{b_m\}(s,\theta)}. \tag{5}$$

The second step of considering pairs of photons is more challenging. Its derivation is in Appendix F. Here, we provide a simplified version. We consider $n_b = 4$ blocks that are uniform and rectangular, with $b_0 = \mathbb{1}_{B_0(n,l)}$. The sensitivity map that expresses the probability that a pair of two antiparallel photons along an LOR are detected by the scanner is

$$\xi(s,\theta) = \max_{m \in \mathbb{M}} \left(\left(1 - e^{-\lambda \mathcal{X}_{\mathbb{1}}\{b_0\}}\right)\left(1 - e^{-\lambda \sum_{k=1}^{n_b-1} \mathcal{X}\{b_0\}(\theta + k\varpi)}\right) + \text{HOI} \right)(\theta + m\varpi) \tag{6}$$

where $\mathcal{X}_{\mathbb{1}}$ is a modified transform that incorporates the FOV and where HOI are potential higher-order interactions that are often negligible (Appendix F).

The mean sensitivity over a domain Ω in the sinogram space can be computed from (6) as

$$\bar{\xi}_\Omega = |\Omega|^{-1} \int_\Omega \xi \, \mathrm{d}s\mathrm{d}\theta. \tag{7}$$

The mean sensitivity of the whole scanner is then $\bar{\xi}_S$ with $S = [-R, R] \times [0, \pi)$. Since the angle of emission of the photons is distributed uniformly in $[0, \pi)$, the mean sensitivity is a good measure of the efficiency of the scanner. At the center of the scanner, the mean sensitivity is $\bar{\xi}_C = \pi^{-1} \int_{[0,\pi)} \xi(s = 0, \theta) \mathrm{d}\theta$, where $C = \{0\} \times [0, \pi)$. More generally, the mean sensitivity of any other point (x, y) in the FOV can be computed by integrating over $\Omega = P_{x,y}$ with

$$P_{x,y} = \{(s, \theta) \mid s = x \sin(\theta) + y \cos(\theta) \text{ and } \theta \in [0, \pi)\}. \tag{8}$$

C. Sensitivity Optimization

Equations (6) and (7) open the door to an optimization of the sensitivity of the scanner. For example, if we focus on geometrical aspects, then we see that ξ depends indirectly on both $\lambda(q)$ and B_0, which in turn is a function of the length l, of the depth h, and of the number n of layers. The mean sensitivity can act as a cost function $\bar{\xi}_S$ in this context and can be maximized in terms of the parameters we just identified.

We discuss three possibilities in this direction.

1) The gradient of ξ can be used in a sort of "sensitivity" analysis to find where the biggest gains lie (Fig. 5). This suggests that the length of the layers contributes mostly to the "stopping" power along the diagonals of the scanner.
2) We can take into account the diminishing return of investment in certain variables, because good tradeoffs are important in proof-of-concept scanners. For example, adding layers increases the sensitivity less and less after $n = 60$ (Fig. 6, left). In fact, the mean sensitivity $\bar{\xi}_S$ saturates at around 25% if one does no more than just adding layers.
3) We can formulate full-fledged optimization problems to reveal the best configuration. Since sensitivity increases monotonically with both the geometric and stopping-power variables, further constraints are necessary to strike a compromise within real-world limitations, such as power consumption, heat dissipation, or budget.

We formulate the problem

$$\arg\max_{q, B_0} \bar{\xi}_S(q, B_0) \text{ subject to } c(q, B_0) = 0 \tag{9}$$

where $c(q, B_0) = 0$ is the constraint. Here, we explored

$$c(B_0) = nl - \text{const.} \tag{10}$$

This keeps the total scanner volume constant, together with the budget, the amount of silicon required, and the power consumption of the system. According to the method of Lagrange multipliers, an optimal tradeoff of (9) under (10) is to set 60 layers of approximately 60 mm (Fig. 6, right).

The conclusion of our study of the sensitivity of the scanner is that 60 layers is good in terms of diminishing returns, and that 60 mm is optimal in terms of the sensitivity. This complements the pitch and depth selected in Section IV.

An increase in $\lambda(q)$ appears as a complementary surefire way to boost the sensitivity. Unfortunately, this comes with design compromises that involve the DOI and the detection process, thereby affecting resolution. We explore these aspects in Section VI by way of simulations. Nevertheless, we performed a preliminary analysis by expanding optimization problem (9) to also include a cost $\bar{\gamma}_S(h) = R^{-1} \int_0^R \gamma(\rho; h) \mathrm{d}\rho$ as a measure of resolution. Find a short report in Appendix G.

VI. Simulations

The aim of the simulations is threefold: to validate the theoretical framework, to study additional parameters (e.g., the addition of bismuth), and to explore the potential quality of reconstructions in the silicon-pixel approach. To these aims, we rely on two different simulations. One (distribution-based

Authorized licensed use limited to: EPFL LAUSANNE. Downloaded on February 10,2025 at 10:31:15 UTC from IEEE Xplore. Restrictions apply.

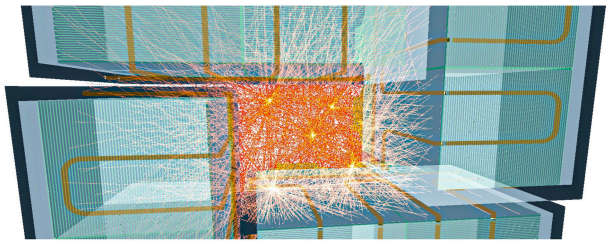

Fig. 7. Simulation of several sources (and the emissions thereof) inside the scanner built in Geant4-Allpix^2 [zoom-in from Fig. 2(c)]. The sources are superimposed for display but were not simulated together for our results.

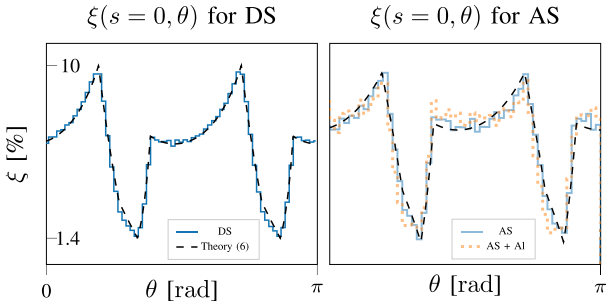

Fig. 8. Theoretical sensitivity [%] compared (left) to DS, and (right) to AS simulations w/wo the aluminum in the cooling blocks.

simulation, DS) is built according to the effects described in Section IV. It encodes them as probability distributions reported in the literature. The other (Geant4-Allpix^2 simulation, AS) is based on detailed physical simulations of particle interactions, but requires more computational power. By comparing the two simulations, we can identify those effects that have the biggest influence. We describe DS and AS in this section, and present results thereof in Section VII. We chose to use FDG in our simulations for two reasons: because it is the most common radiotracer, and because we tailored our pitch to its small MFP. Possible applications are imaging the brain or atherosclerotic plaques [2], [19].

A. Distribution-Based Simulations

The generation of positrons by radioactive decay is simulated according to an inhomogeneous Poisson process with an intensity proportional to the concentration of radiotracer in the phantom image. We sample this process using rejection sampling. The projected path length of the positron until annihilation is drawn from $r(x)$. We sample it as a mixed Laplacian: $C\,\text{Laplace}(0, k_1^{-1}) + (1-C)\,\text{Laplace}(0, k_2^{-1})$, where $C = c/(c+(1-c)k_1/k_2)$ and c, $k_{1,2}$ are fitting constants (e.g., from [36] and [38]). Two photons are then shot forming an angle drawn from a uniform distribution in $[0, \pi)$. An angular error is added on top according to a Gaussian distribution with an FWHM of ϑ. The number of pixels that each photon crosses is drawn from a geometric distribution. If the photon is detected, the event is associated to the center of the nearest pixel. This is fast because all the pixels are on a regular grid, but cannot reproduce scattering. Since the probabilities are independent, we reordered the events to first draw from those for which the most likely outcome is to not progress further.

B. Geant4-Allpix^2 Simulations

We modeled the entire scanner inside the Allpix^2 framework [14]. All silicon detectors and their electronic readout circuits were included. The aluminum cooling blocks and other supporting elements were also added to the simulation (Figs. 2 and 7). The FOV of the scanner was filled with water to simulate the scattering caused by a body.

Allpix^2 interfaces with Geant4, which is the result of a 25-year-long worldwide collaboration that includes CERN and SLAC [13]. Geant4 deploys Monte Carlo methods to simulate the interaction of radiation with matter. The physics models therein are able to reproduce annihilation, photon propagation, scattering, and other electromagnetic phenomena. The acollinearity was simulated by drawing from Gaussians with ϑ of FWHM. The positron range results implicitly from the ion energy spectrum of ^{18}F in Geant4, which peaks at 200 keV (c.f. [36] and [38], see Appendix H). On top of this framework, Allpix^2 takes on the energy deposition from Geant4 and simulates the detection process inside the silicon pixel all the way up to the digitization of the signal (see Section III-C). This includes the propagation of the charge carriers by drift and diffusion, and the signal transfer to the readout circuit. To ward off electronic noise (with a mean of 200 electrons), we set a threshold of 2778 electrons (10 keV) of energy deposition in silicon collected at the pixel electrodes to consider a hit or detection [22]. This is the lower bound of the energy window. The upper bound is the maximal energy among the photon interactions observed, 850 keV, which is substantially below the upper limit of the electronics ($1.3.10^6$ electrons or (4680 keV). The only events we reject are those that activate three (or more) noncontiguous clusters of pixels. These events are rare and usually stem from photons that interact more than once within the scanner.

We validated the Geant4 simulations by comparison to recent literature (see Appendix H).

C. Tomographic Reconstruction of Phantoms

In conformity with the NEMA, reconstructions of simulated point-spread functions (PSFs) were performed using the filtered back-projection (FBP) instead of an iterative method, which can sometimes yield estimates that are too generous [57]. No gap-filling was necessary due to the lack of significant gaps in the sinogram. We approached the step of rebinning the data into parallel rays from the perspective of density estimation rather than interpolation [58], [59], [60]. This is because the volumetric pitch is very small in this scanner and results in point-cloud measurements. We followed [61] to choose the angular sampling $p/2R_{\text{FOV}}$ (Appendix I). Upon reconstruction of a point source through the FBP (ASTRA toolbox [62], [63]), we measured the FWHM of the PSF by finding the two abscissas corresponding to the half maximum by linear interpolation on slices (NEMA).

The inhomogeneity of the sensitivity within the FOV of the scanner is another challenge, and it is more important

Authorized licensed use limited to: EPFL LAUSANNE. Downloaded on February 10,2025 at 10:31:15 UTC from IEEE Xplore. Restrictions apply.

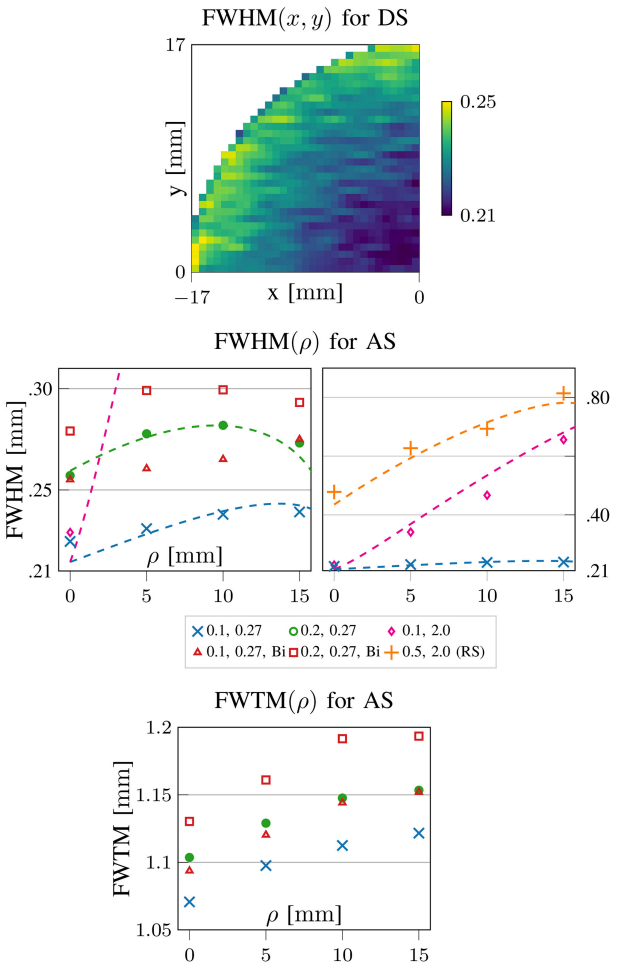

Fig. 9. Top: FWHM over a quarter of the FOV as simulated by DS for a scanner with 0.1 mm of pitch, and 0.27 mm of silicon thickness. Middle: FWHM over the radial offset ρ in AS for combinations of (pitch, silicon thickness) in mm, and with the addition of Bi. The dashed lines are theoretical (Fig. 3). The right graph is a zoom out of the left one, where the orange line (and the crosses) correspond to the values for the RS. A bound on the standard deviation of the error of the FWHM is 0.014 mm. Bottom: FWTMs for the different configurations.

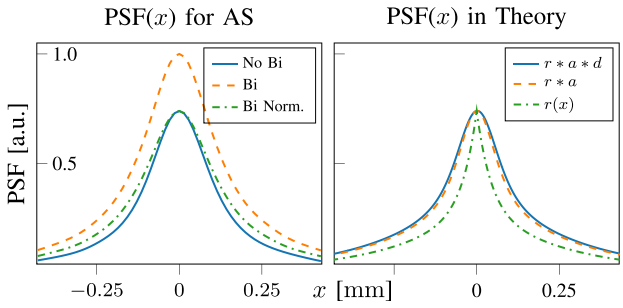

Fig. 10. Slice of the PSF for AS simulations ($p = 0.1$ mm, $R = 17$ mm, and 0.27 of Si) w/wo bismuth, and with further photon-count normalization for shape comparison. Right: The theoretical PSF in (2) as errors compound. We used $c = 0.58$, $k_1 = 23.55$, and $k_2 = 3.75$.

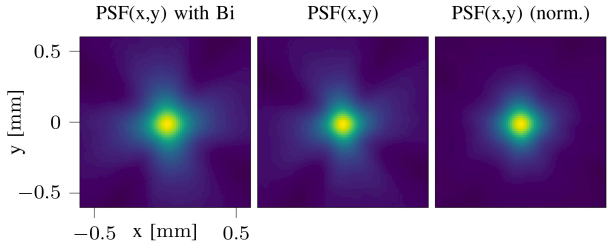

Fig. 11. PSFs. FBP reconstruction (without normalization) of point sources with and without bismuth. The rightmost image (norm.) is normalized using the sensitivity ξ, which eliminates the star-like artifact related to the rectangular shape of the scanner.

to address than in conventional PET because of the rectangular geometry. However, this inhomogeneity does not spoil significantly the amount of information in the sinogram (Appendix J). When applicable according to the NEMA, we compensate for the sensitivity by weighting the density estimation.

We also implemented an iterative reconstruction method to assess the potential of the scanner with a Derenzo phantom. We implemented a custom ordered subset expectation–maximization (OSEM) algorithm [64] that we run on list-mode data. The forward and back projectors are based on the CuPy ray-tracing routine with Joseph-type interpolation provided by parallelproj [65]. For each coincident pair, a ray is traced between the two detectors. We used this reconstruction algorithm to reconstruct the AS simulations, which are completely independent and based on the alternative Monte Carlo approach of Geant4. We set the distance between the center of the rods in the Derenzo phantoms to twice the diameter of the rods. We simulated the phantoms with an activity of 2 MBq for 30 min. This is around half that in [66], but an order of magnitude smaller than in [17]. For our OSEM, we always used a fixed number of 10 iterations of the entire dataset, drawing from 30 different subsets in observance of [57]. We then applied a low-pass Butterworth filter following [67]. We chose a nonregularized OSEM for our evaluation because of its widespread use, but other approaches may further enhance the reconstruction quality [68]. The size of the voxels for most reconstructions was 0.1 mm × 0.1 mm × 0.1 mm, which led to volumes of size (340 × 340 × 440). However, we chose smaller voxels when taking measurements of the resolution such as for the PSF. We did not use attenuation or scattering correction. We did not exploit any TOF information either.

D. Reference Scanner

For the resolution experiments in Section VII, we will compare our proposed scanner design to a hypothetical reference scanner (RS). We designed RS to reproduce the best resolution (~ 0.5 mm at the center) among prototype scanners [17], [18], which is better than those of commercial ones (upward of 1 mm). The RS matches the best parameters in the current state of the art of crystal-based small-animal prototypes (see Section II), but using silicon. Specifically, we used a pitch of $p = 0.5$ mm and a smaller depth of $h = 2$ mm for the RS design. We kept the higher sensitivity of our scanner for the RS.

Authorized licensed use limited to: EPFL LAUSANNE. Downloaded on February 10,2025 at 10:31:15 UTC from IEEE Xplore. Restrictions apply.

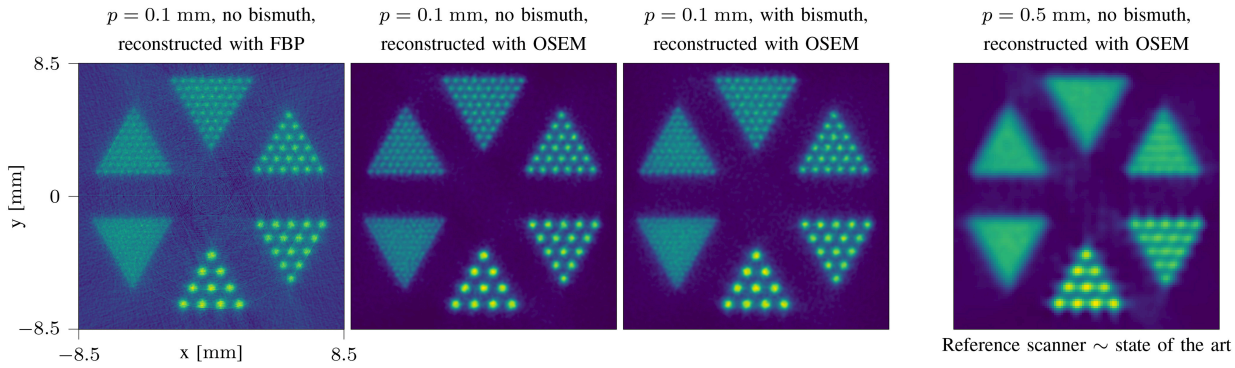

Fig. 12. Reconstructions of a Derenzo phantom in the silicon-pixel scanner using the FBP and an iterative OSEM method. The phantoms are zoomed in. Rod diameters are $\{0.2, 0.25, 0.3, 0.4, 0.5, 0.6\}$ mm. For reference, the minimal size of standard Derenzo rods is usually 1 mm. The first three correspond to the pitch of our scanner, the last is for comparison to the RS that reflects the state of the art in prototypes for small-animal PET ($p = 0.5$ mm, $h = 2$ mm).

VII. Results

A. Sensitivity

We started by studying the sensitivity of the scanner. Both DS and AS were in agreement with our theoretical predictions in (6). More precisely, we found an average relative error of 0.02 (DS) and 0.06 (AS) between theoretical and simulated curves (Fig. 8). This validated our detection model and thus our understanding of the physical processes involved. The small difference between DS and AS indicates that the physical considerations included in DS are the most influential, with scattering playing a minor role. The modeling refinements of the scanner build included in the AS did not interfere in this agreement. This is with the exception of the aluminum casing of the cooling system, which altered the shape of the dips slightly. A mean sensitivity of roughly 3.3% was measured for the whole scanner. The addition of bismuth increased[2] it to 5.0%. The sensitivity of our scanner could be increased by stacking more layers, or by expanding the angular coverage along the axial direction.

B. Resolution

The speed of our DS simulations allowed us to test the resolution across the entire FOV by using many point sources (Fig. 9 top). The results show that resolution follows a radial symmetry and confirms ρ as a good parameterization of FOV resolution. The FWHMs were in line with our theoretical predictions in (3). (Compare the colormap on the left to the values of the blue dashed line on the right.) AS were also in agreement with the theory (Fig. 9 bottom). Precisely, comparing the two theoretical dashed lines with the corresponding simulations (dots and crosses) yielded an average relative error of 0.02. The parallax error appears slightly flatter than predicted. We speculate that this is because of the rectangular shape of the scanner, wherein the LORs remain "more" perpendicular to the detectors as the source moves away from the center; whereas we derived (1) following Fig. 18.

[2]These values were measured over all directions in AS. Only events with two clusters in two different blocks were included in the count. Random coincidences were discarded.

With a pitch of 0.1 and 0.27 mm of silicon thickness, the FWHM was 0.22 mm at the center of the FOV, and 0.24 mm at the edges. The measurements of the FWHM along the other directions in space (axial and tangential) yielded practically the same values ($<$ 0.01 mm differences). The volumetric resolution was thus around 0.01 mm^3. Doubling the pitch to 0.2 mm led to expected results, with the resolution striking an appealing tradeoff at 0.26 mm and 0.27 mm (center, edges). In comparison, the RS had a resolution ranging from 0.48 mm at the center to 0.81 mm at the edges (Fig. 9 bottom, orange plus sign). As expected by design, the results of RS are similar to those in prototype scanners with the best resolution, and twice as good as available commercial scanners. Results for FWTM can be found at the bottom of Fig. 9.

The addition of bismuth worsened the resolution more than we expected from the additional thickness (Fig. 9, middle). It did so with an equivalent FWHM of 0.12 mm. One contributing factor is the relative increase in the number of photoelectric interactions, which deposit more energy and, thus, travel further across the pixels (see Section VII-C). Accordingly, the PSFs were wider with bismuth (Figs. 10 and 11). A pitch of 0.2 mm is thus more convenient (less power consumption) for the bismuth-silicon scanner because the additional error is relatively less significant for the FWHM.

We remark that the fact that DS and AS are completely independent—yet in substantial agreement—can be considered further validation in itself. In our preliminary work [22], we presented Geant4 simulations without acollinearity. Yet we reported a worse resolution because we made a rough approximation without reconstruction. It was based on measuring the distribution of the distance between the simulated LORs and the point source. The scanner design had not been optimized for sensitivity or reconstruction either.

Thus far, all the measurements reported in this section were based on the FBP.

We also studied Derenzo phantoms with the AS (Fig. 12). The reconstructions were performed using either the FBP or the iterative method. The addition of bismuth to the scanner resulted in reconstructions with better contrast, but also with more blur. The scanner was able to recover clearly rods of 0.25 mm both with, and without Bi. We measured the resolvability [69], [70] of the Derenzo rods of 0.25 mm at 96% with

Authorized licensed use limited to: EPFL LAUSANNE. Downloaded on February 10,2025 at 10:31:15 UTC from IEEE Xplore. Restrictions apply.

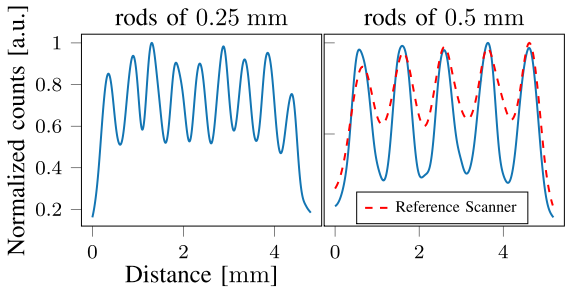

Fig. 13. Left: Slice through one of the inner diagonal lines of 0.25 mm rods in the Derenzo of Fig. 12. For the scanner of $p = 0.1$ mm without bismuth, and for an iterative reconstruction. The VPR is of 0.57 in this example. Right: Slice through 0.5 mm rods comparing our scanner (blue, ratio of 0.25) to the RS (dashed orange, 0.6).

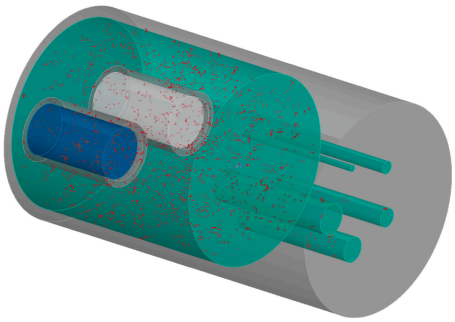

Fig. 14. Simulation of the image-quality phantom. Radioactive material is shown in green, water in blue, air in white, and some annihilation examples are in red. The reconstruction of the phantom is in Appendix K.

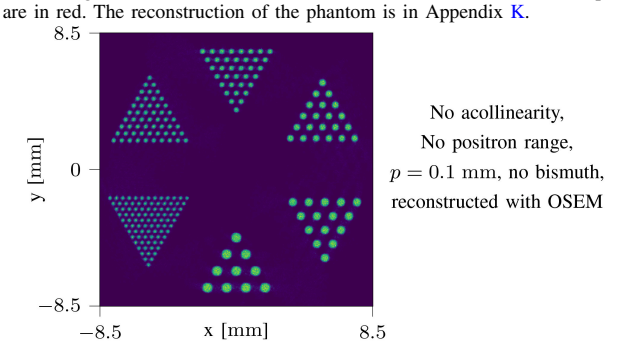

Fig. 15. OSEM reconstruction of a Derenzo phantom in air with no acollinearity and no positron MFP.

a mean valley-to-peak ratio (VPR) of 0.62 (Fig. 13 left). The 0.2 mm rods had an average VPR of 0.77, but only one third of them were above the 0.735 mark dictated by the Rayleigh criterion [69], [71]. We compared the reconstructions of our scanner to that of the hypothetical scanner RS, which combines the best parameters in the state of the art of experimental small-animal PET (see Fig. 12 rightmost, and Fig. 13 right). This scanner was unable to recover rods smaller than 0.5 mm. Note that neither attenuation nor scattering are corrected for in any of the experiments in this manuscript.

For completeness, we simulated and reconstructed an image-quality phantom (Fig. 14). The uniformity had a relative standard deviation of 4.4% (see Appendix K for the reconstruction). The recovery coefficients were $\{0.63, 0.98, 1.01, 1.03, 1.04\} \pm \{0.34, 0.31, 0.31, 0.30, 0.30\}$ for the rods of $\{1, 2, 3, 4, 5\}$ mm. And the spill-over ratio, which is meant to assess the accuracy of scatter correction, was 0.24 ± 0.03 for air and 0.17 ± 0.03 for water. The image-quality results should be interpreted in consideration of the following: these measures have been criticized for their dependency on the algorithm used [69]; the phantom is barely smaller than the scanner diameter-wise and is longer lengthwise; this is a simulation study; and the reconstruction algorithm we used does not correct for scattering and corrects only for the attenuation of the FOV as if it were full of water. We chose this attenuation correction because we could have otherwise achieved a perfect attenuation correction in a simulation. The number of voxels used for these OSEM reconstructions was $(340 \times 340 \times 440)$.

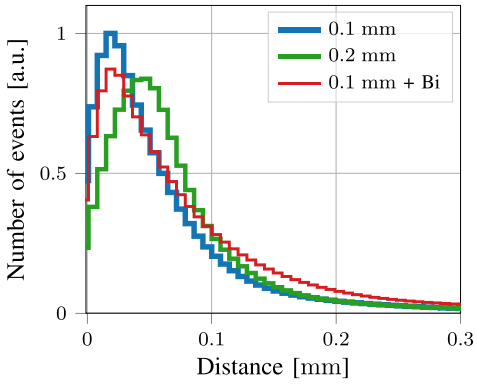

Fig. 16. Histogram of the planar distance (projected onto 1-D) between the location where the photon interacted and the average position of the pixels that were triggered by the traveling photoelectron. For different pixel pitches, and with the addition of Bismuth. The shape of the histograms is reminiscent of a Rayleigh distribution.

C. Scattering and Activity Counts

We next tested the intrinsic resolution of the pixel-detection process. To this end, we performed the AS simulations without MFP nor acolinearity. We also filled the FOV with air instead of water. We reconstructed the PSF at the center of the scanner. The resulting FWHM was of 0.075 mm (0.1 mm with Bi) for a pitch of 0.1 mm; and of 0.11 mm (0.13 mm) for a pitch of 0.2 mm. (Find a Derenzo under these conditions in Fig. 15, cf. Fig. 12.) These results deviate slightly from the ideal half pitch of 0.05 and 0.1 mm, respectively.

This is primarily due to the (random) interpixel walk of the photoelectron resulting from a photon interaction. For the smallest pitch of $p = 0.1$ mm, about 57% of interactions involved a single pixel, whereas 24% involved two pixels. To study the consequences of this in more detail, we projected the distance traveled by the photoelectrons across the pixels. The histograms of these distances (Fig. 16) indicate that most of them travel less than 0.1 mm. Since the interpixel walk enlarges the apparent pitch, a pixel pitch somewhere between 0.1 and 0.2 mm offers the best tradeoff, whereas a smaller

Authorized licensed use limited to: EPFL LAUSANNE. Downloaded on February 10,2025 at 10:31:15 UTC from IEEE Xplore. Restrictions apply.

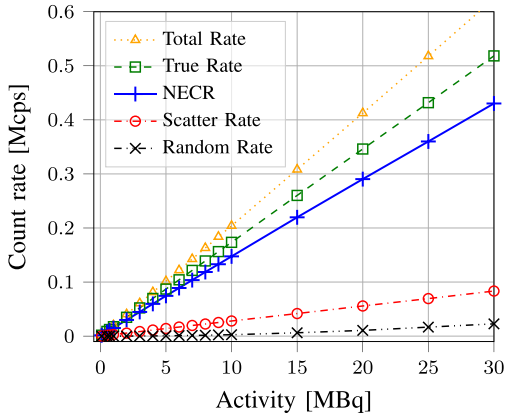

Fig. 17. Count rate as a function of activity with a window of 1 ns. (The timing resolution is of 0.3 ns.)

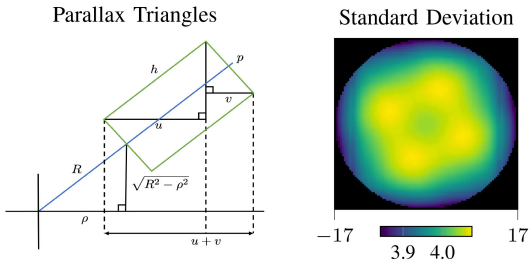

Fig. 18. Left: A detector (slanted rectangle) on a circular scanner is projected onto the axis at an offset ρ. The three right-angled triangles are similar. Right: Scaling $1/\sqrt{\xi_P}$ of the Cramér–Rao bound for the standard deviation in the scanner.

TABLE A2
COMPLEMENTARY INFORMATION FOR TABLE A1. * CRYSTAL SIZE BECAUSE THE FINAL PITCH IS NOT MENTIONED (THE INTERCRYSTAL REFLECTOR ∼ 0.05 MM MIGHT HAVE TO BE ADDED THERETO). † THE PINHOLE DIAMETER IS 0.7 MM FOR THE CRYSTAL PITCH OF 38 MM. ⋆ FROM 20% AROUND THE PHOTOPEAK

Pitch [mm]	Energy Window [keV]	Reference
38†	410-610⋆	[15] (pinhole)
0.42	?	[16]
0.43*	150-	[17]
1	400-600	[18]
0.5	250-750	[21]

pitch would contribute little. This supports the conclusions that we drew from our measurements on the acolinear, rangeless PSF. The addition of Bi to the design worsens the apparent pitch because of the resulting increase in the proportion of photoelectric conversions, which generate photoelectrons of higher energy that walk further. In particular, only 58% of interactions happen through Compton scattering in the scanner with Bi in comparison to 95% without.

On the other hand, interlayer walks are rare. Photoelectrons travel across layers only 1% of the time. This is, in part, due to the FPC. In the few occasions when a layer was crossed by a photoelectron, we observed that the photon had almost always interacted with the innermost layer, which provides a robust criterion for pixel assignment. Note that the loss in resolution stemming from interpixel and interlayer walks could be regarded to be somewhat equivalent to that incurred by intercrystal scattering in standard PET scanners, albeit they happen through different mechanisms.

We then leveraged the full-fledged Monte Carlo simulations (AS) to assess the effect of the placement of the cooling system (Fig. 2). We found that only 3.5% of the photons detected had been previously scattered thereby.

We also used the simulations of our scanner to study the count rate as a function of the activity. In Fig. 17, we present a break down of the rates of the different possible events using a coincidence window of 1 ns. We observe that the random counts constitute a small fraction of the count rate for activities as high as 30 MBq. This puts the noise-equivalent count rate (NECR, see NEMA) in a (practically) linear regime. When comparing this, one should bear in mind the long dead times that are caused by the integration times of some standard PET scanners.

VIII. CONCLUSION AND DISCUSSION

Theory and simulations concur that our proposal of using silicon pixels is promising. The resolution was measured at between 0.22 and 0.24 mm (center, edge) without Bi, and at 0.26–0.27 mm with Bi. The corresponding volumetric resolutions are approximately 0.01 mm^3 and 0.02 mm^3. These results are for FDG; the resolution of radiotracers with bigger positron ranges will be more limited by their corresponding MFP. We have shown that the excellent DOI resolution is one of the spearheads of our scanner design because it increases resolution in multiple ways. The sensitivities are 3.1 and 5.0% with, and without bismuth. (Find a comparison to the state of the art in Section II.) The scanner is under construction (Fig. 2).

The theoretical framework developed to optimize the resolution and sensitivity of our scanner translates well to the design of other scanners. Alternative parameters could also be considered. For instance, a model of heat diffusion could be included as a constraint (or cost function) in (9) to further limit the geometry of the scanner if necessary.

Future efforts will focus on improving the event discrimination of silicon pixels to scale the scanner to a human-compatible size. One could pursue this objective via hardware or via software; for example, by exploiting the energy information with neural networks [31]. Silicon MAPS are under active development. They have been made smaller, thinner, and with better timing [40], [41] than is necessary for our scanner. This comes under different tradeoffs that did not suit our design, but could benefit other architectures. A potential advancement that would improve our small-animal scanner is a reduction of the power consumption that is incurred by more accurate timings because it may enable TOF in such small FOVs.

The MAPS-based design could also be useful in clustered-pinhole PET scanners. These systems do not suffer from the positron range when imaging isotopes with co-emission of prompts, and could thus profit from our small pitches to

Authorized licensed use limited to: EPFL LAUSANNE. Downloaded on February 10,2025 at 10:31:15 UTC from IEEE Xplore. Restrictions apply.

TABLE A1
CHARACTERISTICS OF SOME STATE-OF-THE-ART SMALL-ANIMAL PET SCANNERS WITH RESOLUTIONS CLOSE TO 0.5 MM. VALUES WITH ASTERISKS ARE NOT CLEARLY STATED IN THE WORKS; WE ESTIMATED THEM BASED ON FIGURES THEREIN. VALUES IN PARENTHESIS FOR THE OFF-AXIS-RESOLUTION COLUMN REFER TO THE DISTANCE FROM THE CENTER WHERE THE PSF WAS MEASURED. DAGGERS IN THE DOI REFER TO THE CRYSTAL THICKNESS INSTEAD OF THE DOI RESOLUTION. PARENTHESES IN THE TIMING REFER TO THE WINDOW. FIND THE PITCHES AND THE ENERGY WINDOWS IN TABLE A2

FOV [mm]	Diameter [mm]	Axial coverage [mm]	Resolution [mm]	Res. off axis [mm]	DOI [mm]	Sensitivity [%]	Timing [ns]	Built	Reconstruction	Reference
12	64	9	0.5	?	9.5†	0.29	?	Yes	OSEM	[15] (pinhole)
10*	22.3	14*	0.6	0.75 (4)	5†	0.5	4 (16)	Yes	FBP	[16]
30	61	7	0.5	0.56 (10)*	1.7	1.02	40 (60)	Yes	MLEM	[17]
48	52.5	51.5	0.55	0.8 (15)*	4†	2.84	9.5 (10)	Yes	OSEM	[18]
120	160	254	0.37*	0.4*	1-2	8.9	(4)	Simulated	MLEM	[21]

a greater extent at bigger MFPs. Alternatively, the blurring introduced by the positron range might be able to be mitigated by deconvolution effects given enough counts [37].

Overall, our conclusion is that small-animal PET could benefit from silicon-pixel technology.

APPENDIX

A. Timing Resolution

In [11], we used a pion beam to measure a best timing resolution of 0.02 ns for our MAPS. In the same setting, but at a smaller power consumption similar to that of our scanner, we measured 0.08 ns instead. In our past experiments with a similar MAPS detector [72], the timing resolution that we measured with a ^{22}Na source (511 keV) was twice as good as that measured using a pion beam. The results were 0.07 and 0.13 ns, respectively. Note that we have also measured a timing resolution of 0.14 ns with a ^{90}Sr source (β^- decay with an energy of 546 keV) at similarly low power consumption. We also recall that the timing resolution can be adjusted at the price of power consumption. In addition to this, we are working with a considerable margin: we aim to run our scanner at 0.2 ns of timing resolution. For the simulations, we extended this safety margin even further to 0.3 ns and use a window of 1 ns.

B. Price of the Scanner

A prototype of the scanner is now under construction. The cost of the prototype is of $\sim$ 400 000€. The bulk of the price stems from the MAPS wafers, which costed $\sim$ 300 000€. The rest is divided as follows: 33 000€ for the cooling blocks; 31 000€ for the super-module flex; and 42 000€ for the ensemble of the readout system (control tower, coincidence board, etc.). Costs can be driven down by economies of scale after the prototype phase, especially those of the MAPS. For a rough comparison, the (commercial) price of small-animal PET scanner systems ranges from around 400 000€ to well over 1 000 000€.

C. Readout of the Scanner

To facilitate the integration of the many layers of MAPS in our scanner, we chose to use flip-chip bonding to interface the four detection ASICs of each layer to the backend readout circuit. This allows for a single readout circuit per silicon layer that is thinner and results in a more compact design than with wire bonding. The four ASICs in the layer module are connected in a daisy-chain configuration to be read out by a common line. Each ASIC has a unique ID that is included in the digital output message. This message ($\sim$ 143 bits) is triggered when a particle signal is detected and also contains the energy, timing, and pixel address (25 000 pixels per ASIC). Under an injection dose with a remaining activity of 4.5 MBq at acquisition time, we expect an output of $\sim$ 2.5 Mb/s per layer. This results in $\sim$ 150 Mb/s per each of the four detector blocks (towers) or in $\sim$ 600 Mb/s for the full scanner, which can be interfaced with a standard processing computer. There is still considerable leeway remaining in the design to accommodate higher activities.

D. Geometry

The derivation of (1) is based on the three similar triangles in Fig. 18 left, with $(h/u) = (R/\rho)$ and $(p/v) = (R/\sqrt{R^2-\rho^2})$. One then does $(u+v)/2$.

E. Resolution

1) Variance of the Error Distribution: In (2) of the main text, we obtained the distribution Γ of the final error by convolving the multiple errors. We then computed its FWHM (3). In this section, we compute the variance of this distribution Γ. Notice that the variance of the sum of independent random variables is the sum of their corresponding variances. Therefore, the standard deviation of Γ is

$$\sqrt{r_\sigma^2 + a_\sigma^2 + d_\sigma^2 + m_\sigma^2} \tag{11}$$

where the subscript σ stands for standard deviation of the corresponding distribution, and m for the distribution of the multiplexing error. We remark that the multiplexing term is not relevant to our scanner.

In the literature, (11) is often used to approximate the FWHM. (Think of replacing the subscript σ by FWHM therein.) This is a good approximation when the positron range is negligible (or, instead, all the other errors are). If that is not the case, (11) appears to act as a lower bound when the subscripts are replaced. This is because the exponential cusp of the positron distribution is mollified by the Gaussians.

In our silicon scanner, the positron range is comparable to the other error source. Therefore, we have to use (2) and (3) to compute the FWHM accurately.

Authorized licensed use limited to: EPFL LAUSANNE. Downloaded on February 10,2025 at 10:31:15 UTC from IEEE Xplore. Restrictions apply.

2) Expressions for the Distributions: For documentation, here we clarify the form of the individual error distributions used in the convolutions of (2).

We model the distribution of the positron range as

$$r(x) = \frac{c\exp(-k_1|x|) + (1-c)\exp(-k_2|x|)}{C} \tag{12}$$

where $C/2 = c/k_1 + (1-c)/k_2$ is the normalizing constant. The constants $k_{1,2}$ and c are obtained by fitting the model to simulated data. For the theoretical analysis in Section IV, we used the constants in [36] and [38]. Those in [36] yield an FWHM that appears slightly higher than those in more recent literature [38], but a direct comparison is not possible because the materials are different (see Appendix H). For the comparison between our model for the resolution and the resolution of our simulations (Figs. 9 and 10), we used the values that resulted from fitting our simulations (see Appendix H): $c = 0.58$, $k_1 = 23.55$, and $k_2 = 3.75$.

The distribution of the acollinearity error is given by

$$a(x) = \frac{1}{a_\sigma\sqrt{2\pi}}\exp\left(\frac{-x^2}{2{a_\sigma}^2}\right) \tag{13}$$

with $a_\sigma = a_{\text{FWHM}}/\sqrt{8\ln 2}$. In both DS and AS simulations, we sample from this distribution.

We model the PSF of the detector with the scaled triangle function

$$d(x) = d_{\text{FWHM}}\max(0, 1 - |x/d_{\text{FWHM}}|). \tag{14}$$

This distribution is only used for the theoretical analysis. Neither DS nor AS use it.

F. Derivation of the Sensitivity

The set of detector blocks B_m is indexed by $m \in \mathbb{M} = \mathbb{Z}/n_b\mathbb{Z}$. They are equispaced around the FOV $V \subset \mathbb{R}^d$.

We first present four properties that pertain to the combination of the X-ray transform with the cumulative distribution of the exponential.[3] Consider a subset $C \subset \Omega$. The properties are: $\mathbb{1}_C(1 - \mathrm{e}^{-\lambda\mathcal{X}\{\sum_{\mathbb{M}} b_m\}}) = (1 - \mathrm{e}^{-\lambda\sum_{\mathbb{M}}\mathbb{1}_C\mathcal{X}\{b_m\}})$; $\mathbb{1}_{\mathcal{X}\{\sum_{\mathbb{M}} b_m\}} = \max_{\mathbb{M}}\{\mathbb{1}_{\mathcal{X}\{b_m\}}\}$ for unions; $\mathbb{1}_{\prod_{\mathbb{M}}\mathcal{X}\{b_m\}} = \prod_{\mathbb{M}}\mathbb{1}_{\mathcal{X}\{b_m\}}$ for intersections; and $\mathbb{1}_C(1 - \mathrm{e}^{-\lambda\mathcal{X}\{\sum_{\mathbb{M}} b_m\}}) = |\mathbb{M}| - \sum_{k\in\mathbb{M}}\mathrm{e}^{-\lambda\mathbb{1}_C\sum_{m\in\mathbb{M}\setminus\{k\}}\mathcal{X}\{b_m\}}$ if $\bigcap_{\mathbb{M}}\text{supp}\mathcal{X}\{b_m\} \cap C = \emptyset$.

Notice that the X-ray transform is agnostic to direction. This complicates judging photon-pair interactions. To help us in this endeavor, we build a set $C_0 \subset \mathbb{R}^d$, with $c_0 = \mathbb{1}_{C_0}$, that excludes photons that cross multiple blocks before being absorbed at B_0 yet may retain the other photon of the pair. The rotation of the function by $m\varpi$ is c_m. We also build a set $\mathbb{J}_m \subset \mathbb{M}$ to consider only the necessary blocks. Using these sets in combination with the four properties, we express the probability $\xi_1(s,\theta)$ of a pair of photons emitted in the FOV being detected as an LOR when one of them interacts only once. It reads

$$\xi_1 = \mathbb{1}_{\mathcal{X}\{V\}}\max_{m\in\mathbb{M}}\mathbb{1}^{\mathsf{c}}_{\mathcal{X}\{c_m\}}\left(1 - \mathrm{e}^{-\lambda\mathcal{X}\{b_m\}}\right)\left(1 - \mathrm{e}^{-\lambda\mathcal{X}\{b_{\mathbb{J}_m\setminus\{m\}}\}}\right). \tag{15}$$

[3]We define $\mathbb{1}_{\mathcal{X}\{b_m\}} = \mathbb{1}_{\text{supp}\mathcal{X}\{b_m\}}$ and its complementary $\mathbb{1}^{\mathsf{c}}_{\mathcal{X}\{b_m\}} = (1 - \mathbb{1}_{\mathcal{X}\{b_m\}})$. We use $b_K = \sum_K b_k$ for the indexing set $K \subset \mathbb{Z}$.

We then rewrite (15) as

$$\begin{aligned}\xi_1 &= \mathbb{1}_{\mathcal{X}\{V\}}\max_{m\in\mathbb{M}}\mathbb{1}^{\mathsf{c}}_{\mathcal{X}\{c_0\}(\theta+m\varpi)}\left(1 - \mathrm{e}^{-\lambda\mathcal{X}\{b_0\}(\theta+m\varpi)}\right)\\ &\quad\left(1 - \mathrm{e}^{-\lambda\mathcal{X}\{b_{\mathbb{J}_0\setminus\{0\}}\}(\theta+m\varpi)}\right)\\ &= \max_{m\in\mathbb{M}}\left(\left(1 - \mathrm{e}^{-\lambda\mathcal{X}_{\mathbb{1}}\{b_0\}}\right)\right.\\ &\quad\left.\left(1 - \mathrm{e}^{-\lambda\sum_{k\in\mathbb{J}_0\setminus\{0\}}\mathcal{X}\{b_0\}(\theta+k\varpi)}\right)\right)(\theta + m\varpi)\end{aligned} \tag{16}$$

where $\mathcal{X}_{\mathbb{1}}\{b_0\} = \mathcal{X}\{b_0\}\mathbb{1}_{\text{supp}\mathcal{X}\{V\}\cap(\text{supp}\mathcal{X}\{c_0\})^{\mathsf{c}}}$. Example sets that work in many situations are $c_0 = b_{\mathbb{I}_0}$, $\mathbb{I}_m = \{m - m_b \ldots m-1\}$, $m_b \geq 1$, $\mathbb{J} = \mathbb{I}^{\mathsf{c}}_m$. The expression in terms of the maximum over all rotations is allowed due to the symmetry of the scanner. Each rotation can either lead to a zero or to the correct value. This highlights the role of max in the testing of where each LOR lies with respect to the symmetry. In some special cases with $n_b = 4$, it might be necessary to add an additional term HOI =

$$\left(1 - \mathrm{e}^{-\lambda\mathcal{X}_{\mathbb{1}}\{b_0+b_0(\theta+\varpi)\}}\right)\left(1 - \mathrm{e}^{-\lambda\mathcal{X}\{b_0(\theta+2\varpi)+b_0(\theta+3\varpi)\}}\right) \tag{17}$$

that considers interactions with more than two blocks for each photon of the pair. The total sensitivity is then $\xi = \xi_1 + \text{HOI}$. When there are more blocks, the angles between them are too open for these interactions. The symmetries $\xi(\theta - \pi/2, s) = \xi(\theta, s)$, $\xi(\theta, -s) = \xi(\theta, s)$ can be exploited to reduce the computation cost. We remark that (16) is almost the same in 2-D as in 3-D. In 3-D, $\mathcal{X}_{\mathbb{1}}\{b_0\}$ has to additionally exclude the supp of the X-ray transform of two blocks at the two axial ends.

1) Expression for $\mathcal{X}\{b_m\}$: Each block B_m can be expressed as the transformation $b_m = \mathcal{T}\{c\}$ of a weighting function c on a reference shape C, with $\text{supp}c \subset C$. The transformation $\mathcal{T}$ is the composition rotation$(m\varpi)$ $\circ$ translation$(\mathbf{x}_0)$ $\circ$ scaling(a_x, a_y). The X-ray transform of each block is then $\mathcal{X}\{b_m\}(\theta, s) = \mathcal{X}\{\mathcal{T}\{c\}\} =$

$$\frac{a_\text{x}a_\text{y}}{\kappa}\mathcal{X}\{c\}\left(\arctan\left(\frac{a_\text{y}}{a_\text{x}}\tan(\theta - m\varpi)\right)\right.$$
$$\left.\frac{s - \mathbf{x}_0\cdot(\cos(\theta - m\varpi), \sin(\theta - m\varpi))}{\kappa}\right) \tag{18}$$

where $\kappa = \sqrt{(a_\text{x}\cos(\theta - m\varpi))^2 + (a_\text{y}\sin(\theta - m\varpi))^2}$. This is derived by concatenating the properties of the X-ray transforms. The variables a_x, a_y are the two scaling factors, and $\mathbf{x}_0$ the position of the center of block B_0.

2) Expression for Rectangular Blocks: Notice that a_x, a_y are the lengths of the sides in the case where B_0 is a rectangle, with the reference shape being a square. Consider a uniform block $c = \mathbb{1}_S$, where S is a centered, unit square. We now derive the X-ray transform of the square as a function of our particular parameterization.

We restrict ourselves to $s \in \mathbb{R}_{\geq 0}$, $\theta \in [\pi/4, \pi/2]$. This restriction arises from the square symmetries $\mathcal{X}\{\mathbb{1}_S\}(\theta, s) = \mathcal{X}\{\mathbb{1}_S\}(m\pi/2 + \theta, s)$, $\mathcal{X}\{\mathbb{1}_S\}(\theta, s) = \mathcal{X}\{\mathbb{1}_S\}(\pi/2 - \theta, s)$, and $\mathcal{X}\{\mathbb{1}_S\}(\theta, s) = \mathcal{X}\{\mathbb{1}_S\}(\theta, -s)$. The transform is β^0 (a B-spline of degree 0) at angles perpendicular to the face, and β^1 at the diagonals. Moreover, the X-ray transform has to be continuous

Authorized licensed use limited to: EPFL LAUSANNE. Downloaded on February 10,2025 at 10:31:15 UTC from IEEE Xplore. Restrictions apply.

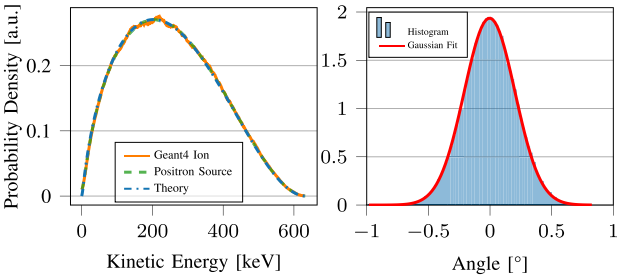

Fig. 19. Left: Energy spectra of ^{18}F. Comparison between the energy spectrum resulting from simulations of the β^+ decay in Geant4, the one that we measure in our AS simulations of a positron source, and those in the LNHB (theory). Right: The angle distribution of only one of the acollinearity angles.

and must preserve the integral. Combining all requirements we get that

$$\mathcal{X}\{\mathbb{1}_S\} = c\left(\beta^0\left(\frac{s}{2s_0}\right) + \mathbb{1}_{s\geq s_0}\beta^1\left(\frac{s-s_0}{s_1}\right)\right) \tag{19}$$

where $c = \csc\theta$ is the intersection length of a line through the origin, $s_0 = (\sin\theta - \cos\theta)/2 = (-\sqrt{2}\sin(\pi/4-\theta)/2)$ is the distance at which the parallel lines reach the first corner, and $s_1 = \cos\theta$ is the distance at which they reach the last.

G. Sensitivity Optimization With Bismuth

In the interest of our study, we augmented the optimization problem to also include a measure of resolution as

$$\arg\max_{h,B_0} \bar{\xi}_S(p, B_0) + \alpha\bar{\gamma}_S(h) \text{ s.t. } c(q, B_0) = 0,\ c_1(h, q) = 0 \tag{20}$$

with $\bar{\gamma}_S(h) = R^{-1}\int_0^R \gamma(\rho; h)\mathrm{d}\rho$ and a parameter $\alpha \in \mathbb{R}_{\geq 0}$ that controls the tradeoff between sensitivity and resolution. We considered increasing $\lambda(q)$ by including bismuth layers sandwiched in-between the silicon layers. Experiments showed that the incorporation of a layer of 0.05 mm to a single detector almost doubled q. We derived the constraint

$$c_1(h, q) = \lambda_{Bi}(h - h_0) + \log(1-q) - \log(1-q_0) = 0 \tag{21}$$

where q_0 and h_0 correspond to the values without Bi. However, setting α proved difficult because we could not find a good characterization of the final reconstruction quality as a function of both parameters. Most importantly, adding bismuth affected the detection process.

H. Simulations

1) Tests of Positron Range and Acollinearity: The positron range in our simulations results from the ion energy spectrum of ^{18}F. We used the spectrum provided by the LNHB.[4] Our simulations coincide with the theory therein, as well as with the energy spectrum that can be obtained from Geant4 by performing very detailed simulations of the β^+ decay of ^{18}F (see Fig. 19, left).

We implemented the acolinearity deviation to follow a 2-D Gaussian distribution of the two (polar and azimuthal) angles defined relative to the case without acolinearity (see Fig. 19, right). We make this remark because it appears that some GATE simulations underestimate the effect of acolinearity by considering that the (combined) amplitude of the angles follows a Gaussian distribution, when it should instead follow a Rayleigh distribution [73].

2) Comparison to the Literature: We validated the Geant4 simulations by comparison to recent literature. The FWHMs of the positron range in cortical bone (63 mm), soft tissue (85 mm), and lung tissue (160 mm) in [38] were close to those of our simulations in the same materials (87, 110, and 170 mm, respectively). We thank Carter et al. [38] for providing the additional details that we needed to establish this comparison. We also compared the FWHM in water (102 mm) of [36] to ours (116 mm). Most of these materials are readily available in Geant4. The fitting of model (12) to the data that we simulated in Geant4 yielded $c = 0.58$, $k_1 = 23.55$, and $k_2 = 3.75$ (cf. [36, Table 1 (corrected units)], [74, Table 1], and [38, Table 2 and Table S1]). Our simulations in water fall around the water in [36] and the soft tissue in [38].

This level of discrepancy is actually common in the literature.[5] See the wide ranges of values in [38, Table S1 in Supplementary], for instance. Another example is that [74, Sec. 3.1] find their FWHM of 160 mm in water to be consistent with the 102 mm of [36]. They explain [74, Sec. 4.1] that the higher FWHM is due to a diffusion-based approximation, as well as to the fixed step size in the computation of energy losses and scattering. This approximation is known as the continuous slowing down approximation (CSDA). It is specially inaccurate when the positron is near the end of its random walk because it has less energy. The PHITS simulation framework, which has several different modes, is used in [38]. Levin and Hoffman [36] used a full model that includes excitation, ionization, multiple Coulomb scattering, and delta electron production. We used Geant4 to implement a similar full model of the physics for better accuracy, albeit at the expense of longer simulation times.

Another possible explanation for the small discrepancies in the literature is the fitting of the model (12), from which the FWHM of the positron is usually derived. This process is sensitive for exponential-like distributions due to their especially narrow cusps (see [38]). Even if small, these differences are still worth exploring because they can be amplified upon convolution with $a(x)$. We therefore looked at the errors introduced by the fitting. We found that fitting the sum of exponentials was quite sensible when we used 10^5 events as is usually done in the literature. We proceeded with 10^7 events instead because the fitting became more stable. Under these conditions, our computation of the analytical FWHM of the fitted exponential yielded the same results as our computation of the FWHM based on a linear interpolation of histogram bins.

Overall, by the shape of our positron range, we expect our results in water to fall somewhere around the water in [36] and the soft tissue in [38]. This is because our water appears close to our soft tissue, which already has a higher FWHM than that

[4] lnhb.fr/home/nuclear-data/nuclear-data-table

[5] All the FWHM values cited in this article correspond to the projection of the MFP onto LORs. That is why they might appear significantly smaller than some numbers reported in the literature for the 3-D distribution [35].

Authorized licensed use limited to: EPFL LAUSANNE. Downloaded on February 10,2025 at 10:31:15 UTC from IEEE Xplore. Restrictions apply.

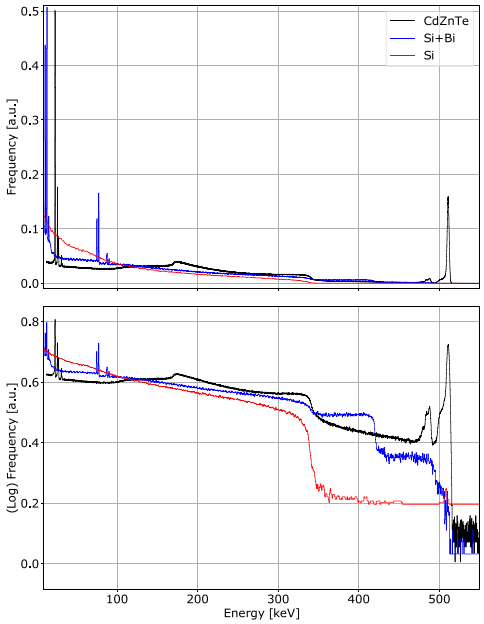

Fig. 20. Energy spectra for the photoelectron clusters generated by an interacting photon in the scanner for three constitutive materials. These materials are CdZnTe, silicon with an additional bismuth layer, and silicon. The bottom graph displays the same data than the top graph, but in logarithmic scale. The CZT has a photopeak at 511keV (where one could compute the typical PET energy resolution), whereas that of silicon alone is very small because most of the interactions that we exploit in our scanner happen through Compton scattering. The silicon bismuth combination displays other photopeaks where the resolution could be computed.

in [38]. We remark that our distributions have a higher FWHM and are less peaky. In principle, this should lead to a worse resolution, thereby making our estimates rather conservative.

3) Implementation Details:

a) DS: We reordered the sequence of events described in Section VI-A to first draw from distributions where the most likely outcome was to not progress further. We chose to run the geometric distribution first, to discard any photons that would penetrate deeper than the longest distance in the scanner. This was possible because the probabilities are independent. The Poisson process was sampled using rejection sampling. The $\pi/2$ rotational symmetry of the scanner was used to increase the efficiency of the code. All these considerations allowed for a simulation speed of $2 \cdot 10^7$ pair-detections per second on an NVIDIA Tesla V100-SXM2 with 32 Gb of memory. The code was developed in-house using CuPy.

To sample from (12) in the DS simulations, we rewrite it as a mixture of two Laplacians. Conversely, for the AS simulations, we simulate the spectrum energy of the positron in Geant4.

b) AS: After thorough optimization of the multithreading process in C++, we achieved a simulation speed of 800 pair-detections per second and thread on CPU (AMD Ryzen 9 5950X).

I. Sinogram Sampling

To choose the optimal sampling rate for reconstruction, we follow [61]. The authors offer a characterization à la Nyquist of the necessary conditions to recover a function from its Radon transform within a target accuracy. This is done by the analysis of the tomographic setups in terms of so-called m-resolving sets, where no nontrivial harmonics vanish up to order m. When we apply the same principles to our scanner design, we obtain intuitive rates to sample the sinogram domain of LORs. To recover details of size c without aliasing, the sampling must be $\Delta s = c/2$ in distance and $\Delta\theta = c/2R_{\text{FOV}}$ in angle, so that $\Delta\theta = \Delta s/R_{\text{FOV}}$. Also similarly to other PET scanners, radial undersampling is expected to generate more artifacts than angular undersampling.

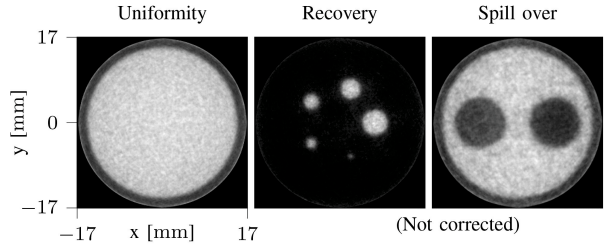

Fig. 21. Reconstruction of the image-quality phantom in Fig. 14. No scatter correction was applied in the algorithm. At 33.5mm of diameter, the phantom fits inside the 34mm of the FOV. (Find a disclaimer in Section VII-B.)

J. Effect of Sensitivity on the Standard Deviation

To assess the effect that the heterogeneous sensitivity of our scanner has on the information gathered in the sinogram, we establish a statistical analysis of the estimation of the concentration.

Let $f(\mathbf{x})$ be the distribution of radiotracer inside the FOV, $\mathbf{x} \in V \subset \mathbb{R}^d$. The emission of photons triggered by nuclear decays behaves like a Poisson process with an intensity proportional to the concentration. The intensity received in the sinogram domain from a point source at $\mathbf{x}$ is $\phi(s,\theta) \propto f(\mathbf{x})\delta_{P_\mathbf{x}}(s,\theta)\xi(s,\theta)/\pi$, where $P_\mathbf{x}$ is defined in (8). This quantity corresponds to the expectation of the Poisson distribution characterizing shot-noise-limited measurements. We used that the angle of emission follows a uniform distribution.

The aim of PET is to recover $f(\mathbf{x})$. The formalism of Cramér–Rao bounds allows us to inspect the variance of an unbiased estimator $\hat{f}(\mathbf{x})$. To this end, we compute the Fisher information as

$$I(f) = \int_\Omega \frac{1}{\phi}\left(\frac{\partial\phi}{\partial f}\right)^2 = \int_P \frac{\phi}{f^2} \propto \frac{\bar{\xi}_P}{\pi f} \tag{22}$$

where we enforced the Poisson likelihood in the first equality [75]. The standard deviation can then be bounded as

$$\sigma_{\hat{f}}^2 \geq I(f)^{-1}. \tag{23}$$

This means that the bound of the standard deviation scales as $1/\sqrt{\bar{\xi}_P}$ (Fig. 18 right), and the bound of the SNR as $\bar{\xi}_P/\bar{\xi}_P^{-1/2} = \bar{\xi}_P^{3/2}$.

We computed the ratio between the bound for the average standard deviation in a reconstruction using the sensitivity of our scanner $\xi(x,y)$ and that for a scanner with uniform sensitivity $\bar{\nu} = |V|^{-1}\int_V \xi(x,y)$. It is $\int_V \xi(x,y)^{-1/2}/\int_V \bar{\nu}^{-1/2} = 1 + 1 \cdot 10^{-3}$. This means that the effect is minimal from the perspective of this statistical detection bound.

Authorized licensed use limited to: EPFL LAUSANNE. Downloaded on February 10,2025 at 10:31:15 UTC from IEEE Xplore. Restrictions apply.

K. Supporting Figures

The energy spectra can be found in Figure 20. The reconstruction of the image phantom can be found in Figure 21.

ACKNOWLEDGMENT

The authors would like to thank V. Taelman and M. Walter for discussions on mouse strains for PET studies. All authors declare that they have no known conflicts of interest in terms of competing financial interests or personal relationships that could have an influence or are relevant to the work reported in this article. They are also grateful to Levin and Hoffman [36] and Carter et al. [38] for providing them the additional details they needed to establish a comparison with their simulations. Some of the authors would like to acknowledge access to the facilities and expertise of the CIBM Center for Biomedical Imaging, a Swiss research center of excellence founded and supported by Lausanne University Hospital (CHUV), University of Lausanne (UNIL), École polytechnique fédérale de Lausanne (EPFL), University of Geneva (UNIGE), and Geneva University Hospitals (HUG).

REFERENCES

[1] A. Gonzalez-Montoro et al., "Evolution of PET detectors and event positioning algorithms using monolithic scintillation crystals," *IEEE Trans. Radiat. Plasma Med. Sci.*, vol. 5, no. 3, pp. 282–305, May 2021.

[2] R. S. Miyaoka and A. L. Lehnert, "Small animal PET: A review of what we have done and where we are going," *Phys. Med. Biol.*, vol. 65, no. 24, Dec. 2020, Art. no. 24TR04. [Online]. Available: https://doi.org/10.1088/1361-6560/ab8f71

[3] J. Du, X. Bai, and S. R. Cherry, "Performance comparison of depth-encoding detectors based on dual-ended readout and different SiPMs for high-resolution PET applications," *Phys. Med. Biol.*, vol. 64, no. 15, Aug. 2019, Art. no. 15NT03. [Online]. Available: https://dx.doi.org/10.1088/1361-6560/ab1c37

[4] I. Mohammadi, I. F. C. Castro, P. M. M. Correia, A. L. M. Silva, and J. F. C. A. Veloso, "Minimization of parallax error in positron emission tomography using depth of interaction capable detectors: Methods and apparatus," *Biomed. Phys. Eng. Exp.*, vol. 5, no. 6, Oct. 2019, Art. no. 62001. [Online]. Available: https://dx.doi.org/10.1088/2057-1976/ab4a1b

[5] J. Jakůbek, "Semiconductor pixel detectors and their applications in life sciences," *J. Instrum.*, vol. 4, no. 3, Mar. 2009, Art. no. P03013. [Online]. Available: https://dx.doi.org/10.1088/1748-0221/4/03/P03013

[6] N. Wermes, "Pixel detectors for charged particles," *Nuclear Instrum. Methods Phys. Res. Sect. A, Accelerat., Spectrometers, Detect. Assoc. Equip.*, vol. 604, no. 1-2, pp. 370–379, Jun. 2009.

[7] E. H. M. Heijne, "History and future of radiation imaging with single quantum processing pixel detectors," *Radiat. Meas.*, vol. 140, Jan. 2021, Art. no. 106436. [Online]. Available: https://www.sciencedirect.com/science/article/pii/S1350448720302146

[8] M. Garcia-Sciveres and N. Wermes, "A review of advances in pixel detectors for experiments with high rate and radiation," *Rep. Prog. Phys.*, vol. 81, no. 6, May 2018, Art. no. 66101. [Online]. Available: https://dx.doi.org/10.1088/1361-6633/aab064

[9] I. Perić, "A novel monolithic pixelated particle detector implemented in high-voltage CMOS technology," *Nuclear Instrum. Methods Phys. Res. Sect. A, Accelerat., Spectrometers, Detect. Assoc. Equip.*, vol. 582, no. 3, pp. 876–885, Dec. 2007. [Online]. Available: https://www.sciencedirect.com/science/article/pii/S0168900207015914

[10] G. Iacobucci, L. Paolozzi, and P. Valerio, "Monolithic picosecond silicon pixel sensors for future physics: Experiments and applications," *IEEE Instrum. Meas. Mag.*, vol. 24, no. 9, pp. 5–11, Dec. 2021.

[11] S. Zambito et al., "20 ps time resolution with a fully-efficient monolithic silicon pixel detector without internal gain layer," *J. Instrum.*, vol. 18, no. 03, Mar. 2023, Art. no. P03047. [Online]. Available: https://dx.doi.org/10.1088/1748-0221/18/03/P03047

[12] L. Paolozzi et al., "Time resolution and power consumption of a monolithic silicon pixel prototype in SiGe BiCMOS technology," *J. Instrum.*, vol. 15, no. 11, Nov. 2020, Art. no. P11025. [Online]. Available: https://dx.doi.org/10.1088/1748-0221/15/11/P11025

[13] S. Agostinelli et al., "Geant4—A simulation toolkit," *Nuclear Instrum. Methods Phys. Res. Sect. A, Accelerat., Spectrometers, Detect. Assoc. Equip.*, vol. 506, no. 3, pp. 250–303, Jul. 2003. [Online]. Available: https://www.sciencedirect.com/science/article/pii/S0168900203013688

[14] S. Spannagel et al., "Allpix2: A modular simulation framework for silicon detectors," *Nuclear Instrum. Methods Phys. Res. Sect. A, Accelerat., Spectrometers, Detect. Assoc. Equip.*, vol. 901, pp. 164–172, Sep. 2018. [Online]. Available: https://www.sciencedirect.com/science/article/pii/S0168900218307411

[15] K. Miwa et al., "Performance characteristics of a novel clustered multi-pinhole technology for simultaneous high-resolution SPECT/PET," *Ann. Nuclear Med.*, vol. 29, no. 5, pp. 460–466, Jun. 2015. [Online]. Available: https://doi.org/10.1007/s12149-015-0966-6

[16] S. Yamamoto et al., "Development of ultrahigh resolution Si-PM-based PET system using 0.32mm pixel scintillators," *Nuclear Instrum. Methods Phys. Res. Sect. A, Accelerat., Spectrometers, Detect. Assoc. Equip.*, vol. 836, pp. 7–12, Nov. 2016. [Online]. Available: https://www.sciencedirect.com/science/article/pii/S0168900216308634

[17] Y. Yang et al., "A prototype high-resolution small-animal PET scanner dedicated to mouse brain imaging," *J. Nuclear Med.*, vol. 57, no. 7, pp. 1130–1135, Jul. 2016. [Online]. Available: https://jnm.snmjournals.org/content/57/7/1130

[18] H. G. Kang et al., "Submillimeter-resolution PET for high-sensitivity mouse brain imaging," *J. Nuclear Med.*, vol. 64, no. 6, pp. 978–985, Jun. 2023. [Online]. Available: https://jnm.snmjournals.org/content/64/6/978

[19] R. K. Tangirala, E. M. Rubin, and W. Palinski, "Quantitation of atherosclerosis in murine models: correlation between lesions in the aortic origin and in the entire aorta, and differences in the extent of lesions between sexes in LDL receptor-deficient and apolipoprotein E-deficient mice," *J. Lipid Res.*, vol. 36, no. 11, pp. 2320–2328, Nov. 1995.

[20] V. Doyon et al., "First PET investigation of the human brain at 2 μL resolution with the ultra-high-resolution (UHR) scanner," *J. Nuclear Med.*, vol. 64, no. 1, pp. P726–P726, Jun. 2023. [Online]. Available: https://jnm.snmjournals.org/content/64/supplement_1/P726

[21] Y. Lai et al., "H2RSPET: A 0.5 mm resolution high-sensitivity small-animal PET scanner, a simulation study," *Phys. Med. Biol.*, vol. 66, no. 6, Mar. 2021, Art. no. 65016. [Online]. Available: https://doi.org/10.1088/1361-6560/abe558

[22] F. Cadoux et al., "The 100muPET project: A small-animal PET scanner for ultra-high resolution molecular imaging with monolithic silicon pixel detectors," in *Proc. 15th Pisa Meet. Adv. Detect. Nuclear Instrum. Methods Phys. Res. Sect. A*, 2023, Art. no. 167952. [Online]. Available: https://www.sciencedirect.com/science/article/pii/S016890022201244X

[23] J. Missimer, Z. Madi, M. Honer, C. Keller, A. Schubiger, and S.-M. Ametamey, "Performance evaluation of the 16-module quad-HIDAC small animal PET camera," *Phys. Med. Biol.*, vol. 49, no. 10, p. 2069, May 2004. [Online]. Available: https://dx.doi.org/10.1088/0031-9155/49/10/016

[24] G. Di Domenico et al., "SiliPET: An ultra-high resolution design of a small animal PET scanner based on stacks of double-sided silicon strip detector," *Nuclear Instrum. Methods Phys. Res. Sect. A, Accelerat., Spectrometers, Detect. Assoc. Equip.*, vol. 571, no. 1, pp. 22–25, Feb. 2007. [Online]. Available: https://www.sciencedirect.com/science/article/pii/S0168900206018183

[25] Z. Gu et al., "NEMA NU-4 performance evaluation of PETbox4, a high sensitivity dedicated PET preclinical tomograph," *Phys. Med. Biol.*, vol. 58, no. 11, p. 3791, May 2013. [Online]. Available: https://dx.doi.org/10.1088/0031-9155/58/11/3791

[26] S. España, R. Marcinkowski, V. Keereman, S. Vandenberghe, and R. V. Holen, "DigiPET: Sub-millimeter spatial resolution small-animal PET imaging using thin monolithic scintillators," *Phys. Med. Biol.*, vol. 59, no. 13, p. 3405, Jun. 201. [Online]. Available: https://dx.doi.org/10.1088/0031-9155/59/13/3405

[27] J. Müller et al., "Multi-modality bedding platform for combined imaging and irradiation of mice," *Biomed. Phys. Eng. Exp.*, vol. 6, no. 3, Apr. 2020, Art. no. 37003. [Online]. Available: https://dx.doi.org/10.1088/2057-1976/ab79f1

[28] R. Chakraborty, H. n. Park, C. C. Tan, P. Weiss, M. C. Prunty, and M. T. Pardue, "Association of body length with ocular parameters in mice," *Optometry Vis. Sci.*, vol. 94, no. 3, p. 387, Mar. 2017. [Online]. Available: https://journals.lww.com/optvissci/abstract/2017/03000/association_of_body_length_with_ocular_parameters.14.aspx

Authorized licensed use limited to: EPFL LAUSANNE. Downloaded on February 10,2025 at 10:31:15 UTC from IEEE Xplore. Restrictions apply.

[29] C. Ritzer, P. Hallen, D. Schug, and V. Schulz, "Intercrystal scatter rejection for pixelated PET detectors," *IEEE Trans. Radiat. Plasma Med. Sci.*, vol. 1, no. 2, pp. 191–200, Mar. 2017. [Online]. Available: https://ieeexplore.ieee.org/document/7843591

[30] Z. Gu, R. Taschereau, N. T. Vu, D. L. Prout, J. Lee, and A. F. Chatziioannou, "Performance evaluation of HiPET, a high sensitivity and high resolution preclinical PET tomograph," *Phys. Med. Biol.*, vol. 65, no. 4, Feb. 2020, Art. no. 45009. [Online]. Available: https://dx.doi.org/10.1088/1361-6560/ab6b44

[31] S. Lee and J. S. Lee, "Experimental evaluation of convolutional neural network-based inter-crystal scattering recovery for high-resolution PET detectors," *Phys. Med. Biol.*, vol. 68, no. 9, Apr. 2023, Art. no. 95017. [Online]. Available: https://dx.doi.org/10.1088/1361-6560/accacb

[32] K. Ishii et al., "First achievement of less than 1 mm FWHM resolution in practical semiconductor animal PET scanner," *Nuclear Instrum. Methods Phys. Res. Sect. A, Accelerat., Spectrometers, Detect. Assoc. Equip.*, vol. 576, no. 2, pp. 435–440, Jun. 2007. [Online]. Available: https://www.sciencedirect.com/science/article/pii/S0168900207004962

[33] S. Abbaszadeh, Y. Gu, P. D. Reynolds, and C. S. Levin, "Characterization of a sub-assembly of 3D position sensitive cadmium zinc telluride detectors and electronics from a sub-millimeter resolution PET system," *Phys. Med. Biol.*, vol. 61, no. 18, pp. 6733–6753, Sep. 2016.

[34] J. R. Stickel and S. R. Cherry, "High-resolution PET detector design: Modelling components of intrinsic spatial resolution," *Phys. Med. Biol.*, vol. 50, no. 2, p. 179, Dec. 2004. [Online]. Available: https://dx.doi.org/10.1088/0031-9155/50/2/001

[35] W. W. Moses, "Fundamental limits of spatial resolution in PET," *Nuclear Instrum. Methods Phys. Res. Sect. A, Accelerat., Spectrometers, Detect. Assoc. Equip.*, vol. 648, pp. S236–S240, Aug. 2011. [Online]. Available: https://www.sciencedirect.com/science/article/pii/S0168900210026276

[36] C. S. Levin and E. J. Hoffman, "Calculation of positron range and its effect on the fundamental limit of positron emission tomography system spatial resolution," *Phys. Med. Biol.*, vol. 44, no. 3, pp. 781–799, Jan. 1999. [Online]. Available: https://doi.org/10.1088/0031-9155/44/3/019

[37] S. E. Derenzo, "Mathematical removal of positron range blurring in high resolution tomography," *IEEE Trans. Nuclear Sci.*, vol. 33, no. 1, pp. 565–569, Feb. 1986.

[38] L. M. Carter et al., "The impact of positron range on PET resolution, evaluated with phantoms and PHITS monte carlo simulations for conventional and non-conventional radionuclides," *Mol. Imag. Biol.*, vol. 22, no. 1, pp. 73–84, Feb. 2020. [Online]. Available: https://www.ncbi.nlm.nih.gov/pmc/articles/PMC6805144/

[39] P. Colombino, B. Fiscella, and L. Trossi, "Study of positronium in water and ice from 22 to-144 C by annihilation quanta measurements," *Il Nuovo Cimento*, vol. 38, no. 2, pp. 707–723, Jul. 1965. [Online]. Available: https://doi.org/10.1007/BF02748591

[40] M. Mager, "ALPIDE, the monolithic active pixel sensor for the ALICE its upgrade," *Nuclear Instrum. Methods Phys. Res. Sect. A, Accelerat., Spectrometers, Detect. Assoc. Equip.*, vol. 824, pp. 434–438, Jul. 2016. [Online]. Available: https://www.sciencedirect.com/science/article/pii/S0168900215011122

[41] ALICE ITS project, "First demonstration of in-beam performance of bent monolithic active pixel sensors," *Nuclear Instrum. Methods Phys. Res. Sect. A, Accelerat., Spectrometers, Detect. Assoc. Equip.*, vol. 1028, Apr. 2022, Art. no. 166280. [Online]. Available: https://www.sciencedirect.com/science/article/pii/S0168900221011098

[42] S. E. Derenzo, T. F. Budinger, R. H. Huesman, J. L. Cahoon, and T. Vuletich, "Imaging properties of a positron tomograph with 280 BGO crystals," *IEEE Trans. Nuclear Sci.*, vol. 28, no. 1, pp. 81–89, Feb. 1981.

[43] T. F. Budinger, "Time-of-flight positron emission tomography: Status relative to conventional PET," *J. Nuclear Med.*, vol. 24, no. 1, pp. 73–78, Jan. 1983. [Online]. Available: https://jnm.snmjournals.org/content/24/1/73

[44] J. H. Hubbell, W. J. Veigele, E. A. Briggs, R. T. Brown, D. T. Cromer, and R. J. Howerton, "Atomic form factors, incoherent scattering functions, and photon scattering cross sections," *J. Phys. Chem. Ref. Data*, vol. 4, no. 3, pp. 471–538, Jul. 1975. [Online]. Available: https://doi.org/10.1063/1.555523

[45] "NIST: X-ray mass attenuation coefficients-section 2." Accessed: Nov. 20, 2022. [Online]. Available: https://physics.nist.gov/PhysRefData/XrayMassCoef/chap2.html

[46] H. Zaidi and M.-L. Montandon, "Scatter compensation techniques in PET," *PET Clin.*, vol. 2, no. 2, pp. 219–234, Apr. 2007.

[47] Q. Bao, D. Newport, M. Chen, D. B. Stout, and A. F. Chatziioannou, "Performance evaluation of the Inveon dedicated PET preclinical tomograph based on the NEMA NU-4 standards," *J. Nuclear Med.*, vol. 50, no. 3, pp. 401–408, Mar. 2009. [Online]. Available: https://jnm.snmjournals.org/content/50/3/401

[48] H. Sawada, J. Z. Chen, B. C. Wright, J. J. Moorleghen, H. S. Lu, and A. Daugherty, "Ultrasound imaging of the thoracic and abdominal aorta in mice to determine aneurysm dimensions," *J. Vis. Exp.*, no. 145, Mar. 2019, Art. no. e59013, doi: 10.3791/59013.

[49] C. J. Goergen et al., "In vivo quantification of murine aortic cyclic strain, motion, and curvature: Implications for abdominal aortic aneurysm growth," *J. Mag. Reson. Imag.*, vol. 32, no. 4, pp. 847–858, 2010. [Online]. Available: https://onlinelibrary.wiley.com/doi/abs/10.1002/jmri.22331

[50] D. J. Lloyd et al., "A volumetric method for quantifying atherosclerosis in mice by using MicroCT: Comparison to en face," *Plos One*, vol. 6, no. 4, Apr. 2011, Art. no. e18800. [Online]. Available: https://journals.plos.org/plosone/article?id=10.1371/journal.pone.0018800

[51] J. Jiao et al., "Direct parametric reconstruction with joint motion estimation/correction for dynamic brain PET data," *IEEE Trans. Med. Imag.*, vol. 36, no. 1, pp. 203–213, Jan. 2017.

[52] M. Thamm et al., "Intrinsic respiratory gating for simultaneous multi-mouse μCT imaging to assess liver tumors," *Front. Med.*, vol. 9, Jul. 2022, Art. no. 878966. [Online]. Available: https://www.frontiersin.org/articles/10.3389/fmed.2022.878966

[53] D. A. Rivera, A. E. Buglione, and C. B. Schaffer, "MousePZT: A simple, reliable, low-cost device for vital sign monitoring and respiratory gating in mice under anesthesia," bioRxiv, Preprint, Feb. 2023. [Online]. Available: https://www.biorxiv.org/content/10.1101/2023.02.23.529566v1

[54] S. A. Nehmeh et al., "Effect of respiratory gating on quantifying PET images of lung cancer," *J. Nuclear Med.*, vol. 43, no. 7, pp. 876–881, Jul. 2002. [Online]. Available: https://jnm.snmjournals.org/content/43/7/876

[55] M. Grasruck et al., "Motion gated small animal imaging with a flat-panel CT," in *Proc. Med. Imag., Phys. Med. Imag.*, 2008, pp. 1384–1391. [Online]. Available: https://www.spiedigitallibrary.org/conference-proceedings-of-spie/6913/69134D/Motion-gated-small-animal-imaging-with-a-flat-panel-CT/10.1117/12.769386.full

[56] S. I. Kwon et al., "Ultrafast timing enables reconstruction-free positron emission imaging," *Nat. Photon.*, vol. 15, no. 12, pp. 914–918, Dec. 2021. [Online]. Available: https://www.nature.com/articles/s41566-021-00871-2

[57] K. Gong, S. R. Cherry, and J. Qi, "On the assessment of spatial resolution of PET systems with iterative image reconstruction," *Phys. Med. Biol.*, vol. 61, no. 5, p. N193, Feb. 2016. [Online]. Available: https://dx.doi.org/10.1088/0031-9155/61/5/N193

[58] A. Boquet-Pujadas, P. del Aguila Pla, and M. Unser, "PET rebinning with regularized density splines," in *Proc. IEEE 20th Int. Symp. Biomed. Imag. (ISBI)*, 2023, pp. 1–4.

[59] P. del Aguila Pla, A. Boquet-Pujadas, and J. Jaldén, "Convex quantization preserves logconcavity," *IEEE Signal Process. Lett.*, vol. 29, pp. 2697–2701, 2022.

[60] A. Boquet-Pujadas, P. d. A. Pla, and M. Unser, "Sensitivity-Aware Density Estimation in Multiple Dimensions," *IEEE Trans. Pattern Anal. Mach. Intell.*, early access, Apr. 12, 2024, doi: 10.1109/TPAMI.2024.3388370. [Online]. Available: https://ieeexplore.ieee.org/document/10497882

[61] F. Natterer, "3. Sampling and resolution," in *The Mathematics of Computerized Tomography* (Classics in Applied Mathematics). Philadelphia, PA, USA: Soc. Ind. Appl. Math., Jan. 2001, pp. 54–84. [Online]. Available: https://epubs.siam.org/doi/10.1137/1.9780898719284.ch3

[62] W. van Aarle et al., "The ASTRA toolbox: A platform for advanced algorithm development in electron tomography," *Ultramicroscopy*, vol. 157, pp. 35–47, Oct. 2015. [Online]. Available: https://www.sciencedirect.com/science/article/pii/S0304399115001060

[63] W. v. Aarle et al., "Fast and flexible X-ray tomography using the ASTRA toolbox," *Opt. Exp.*, vol. 24, no. 22, pp. 25129–25147, Oct. 2016. [Online]. Available: https://opg.optica.org/oe/abstract.cfm?uri=oe-24-22-25129

[64] H. Hudson and R. Larkin, "Accelerated image reconstruction using ordered subsets of projection data," *IEEE Trans. Med. Imag.*, vol. 13, no. 4, pp. 601–609, Dec. 1994.

[65] G. Schramm and K. Thielemans, "PARALLELPROJ–an open-source framework for fast calculation of projections in tomography," 2023, *arXiv:2212.12519*.

[66] J. Liu, Q. Liu, J.-C. Chen, and D. Wang, "A prototype ultra-high-resolution small-animal PET system," *J. Nuclear Med.*, vol. 62, no. 1, p. 184, May 2021. [Online]. Available: https://jnm.snmjournals.org/content/62/supplement_1/184

Authorized licensed use limited to: EPFL LAUSANNE. Downloaded on February 10,2025 at 10:31:15 UTC from IEEE Xplore. Restrictions apply.

[67] E. Wikberg, M. van Essen, T. Rydén, J. Svensson, P. Gjertsson, and P. Bernhardt, "Evaluation of reconstruction methods and image noise levels concerning visual assessment of simulated liver lesions in ^{111}In-octreotide SPECT imaging," *EJNMMI Phys.*, vol. 10, no. 1, p. 36, Jun. 2023. [Online]. Available: https://doi.org/10.1186/s40658-023-00557-4

[68] M. Millardet et al., "A multiobjective comparative analysis of reconstruction algorithms in the context of low-statistics ^{90}Y-PET imaging," *IEEE Trans. Radiat. Plasma Med. Sci.*, vol. 6, no. 6, pp. 629–640, Jul. 2022. [Online]. Available: https://ieeexplore.ieee.org/document/9610126/authors

[69] P. Hallen, D. Schug, and V. Schulz, "Comments on the NEMA NU 4-2008 standard on performance measurement of small animal positron emission tomographs," *EJNMMI Phys.*, vol. 7, no. 1, p. 12, Feb. 2020. [Online]. Available: https://doi.org/10.1186/s40658-020-0279-2

[70] H. G. Kang et al., "Initial results of a mouse brain PET insert with a staggered 3-layer DOI detector," *Phys. Med. Biol.*, vol. 66, no. 21, Nov. 2021, Art. no. 215015. [Online]. Available: https://dx.doi.org/10.1088/1361-6560/ac311c

[71] T. S. McKechnie, "Telescope resolution and optical tolerance specifications," in *General Theory of Light Propagation and Imaging Through the Atmosphere*, T. S. McKechnie, Ed., Cham, Switzerland: Springer Int. Publ., 2016, pp. 405–464. [Online]. Available: https://doi.org/10.1007/978-3-319-18209-4_14

[72] D. Hayakawa, "Development of the thin TOF-PET scanner based on fast timing monolithic silicon pixel sensors," Ph.D. dissertation, Dept. Physique Nucléaire et Corpusculaire, Université de Genéve, Geneva, Switzerland, 2020.

[73] M. Toussaint, F. Loignon-Houle, E. Auger, J.-P. Dussault, and R. Lecomte, "Pitfall in the implementation of acollinearity in PET monte carlo simulation softwares," in *Proc. IEEE Nuclear Sci. Symp., Med. Imag. Conf. Int. Symp. Room-Temp. Semicond. Detect. (NSS MIC RTSD)*, 2023, pp. 1–1. [Online]. Available: https://ieeexplore.ieee.org/document/10338458

[74] H. Peng and C. S. Levin, "Study of PET intrinsic spatial resolution and contrast recovery improvement for PET/MRI systems," *Phys. Med. Biol.*, vol. 57, no. 9, p. N101, Apr. 2012. [Online]. Available: https://dx.doi.org/10.1088/0031-9155/57/9/N101

[75] C. Cloquet, S. Goldman, and M. Defrise, "Cramer–Rao bound for gated PET," in *Proc. IEEE Nuclear Sci. Symp. Med. Imag. Conf.*, Knoxville, TN, USA, 2010, pp. 2267–2272.

Authorized licensed use limited to: EPFL LAUSANNE. Downloaded on February 10,2025 at 10:31:15 UTC from IEEE Xplore. Restrictions apply.